Quantitative three-dimensional imaging in cancer research using optical computed tomography

Ciara McErlean

Thursday 3rd December, 2015

Contents

2 Methods and Characterisation

2.1 Optical CT Materials and Methods

The optical CT system was originally designed to provide radiation dosimetry using the solid radiochromic plastic PRESAGE®. It has now been adapted to also allow imaging of *ex vivo* tissue samples. The system is broadly the same for both applications, with some minor hardware differences. The high-quality and uniform dosimetric samples were used to help develop the system and scanning procedures before imaging the more heterogeneous tissue samples.

2.1.1 Hardware

The main components of the ICR optical CT system are shown in Figure 2.1. This system is based on the one described in [Doran et al., 2013b] with several improvements and adaptations.

A CMOS (complementary metal-oxide semiconductor) camera (Zyla sCMOS, Andor Technology PLC, Belfast, UK) with a large pixel array and fast frame-rate allows for much faster imaging with larger projection matrix size than previously reported systems. Recent advances in CMOS and CCD (charge-coupled device) camera technology means that higher quality optical CT systems can be built cheaply. The scanning speed was also greatly improved by the addition of a new PC with 256 GB RAM (Dell), which controls acquisition and performs reconstruction.

Two illumination sources are used, depending on the application. A flat-panel red light-emitting diode (LED) (PHLOX-LEDR-BL-100 × 100-S-Q-1R-24V, Phlox, Aix-en-Provence, France), with a wavelength of 633 nm provides uniform lighting appropriate for imaging PRESAGE®, which has a strong absorption peak at 632 nm. For tissue imaging the wavelength most appropriate for each sample is provided through the use of a new broadband white light source (SugarCUBE LED Illuminator, Nathaniel Group Inc., VT, USA) and tunable filter (VariSpec, PerkinElmer, Inc., MA, USA).

Light is collected by an imaging lens system made up of components of the modular 'Z16 APO' zoom system (Leica Microsystems GmbH, Wetzlar, Germany, see [Doran et al., 2010a] for details). The use of a zoom lens allows manual adjustment of the focus, depth-of-field and magnification giving this system flexibility to image a range of sample sizes.

Samples are suspended from a rotation stage (PRS-110 ZSS43, PI miCos GmbH, Eschbach, Germany) in a glass matching tank (Part 704-002-40-10, Hellma GmbH, Müllheim, Germany). The matching tank is filled with 'matching liquid' with a refractive index (RI) close to that of the sample, avoiding refraction at the sample surface. For initial measurements the rotation stage was supported on a large optical post. In an updated system this post was replaced with an Integrated Long Travel Stage (LTS-300/M, Thorlabs Ltd., Ely, UK) which allows accurate and reproducible vertical positioning of samples.

In collaboration with the ICR workshop, two custom mounting systems have been developed for dosimetry and tissue samples. Samples are attached to the rotation stage via sample holder 'caps' which fit reproducibly into the sample holder. PRESAGE® samples can be glued into caps, meaning the samples are in the same orientation for every scan allowing easy registration between scans (see Figure 2.2). Tissue sample caps have a flat base onto which gel-embedded tissue can be glued for stable rotation (see Figure 2.3).

The rotation stage is mounted on a micrometer stage allowing precise alignment of the centre-of-rotation (COR) with the centre of the projection images. If the COR is not aligned with the central pixel column, then the sample will appear to drift across the screen and projection data will not be consistent for all angles. [Guo et al., 2006] The tissue mount has two additional stages controlling the position of the sample holder, giving the flexibility to position samples on the COR. This correction is needed if samples aren't in the exact centre of the sample cap.

An additional Long Travel Stage (LTS-150/M, Thorlabs LTD., Ely, UK) allows accurate positioning of both the rotation stage and matching tank along the optical axis. In general the manual focus ring on the zoom lens was left in a fixed position and the LTS stage was used to position the COR at the focal plane, giving more repeatable imaging. The procedure for aligning the COR with the focal plane is given in Section 2.2.3.

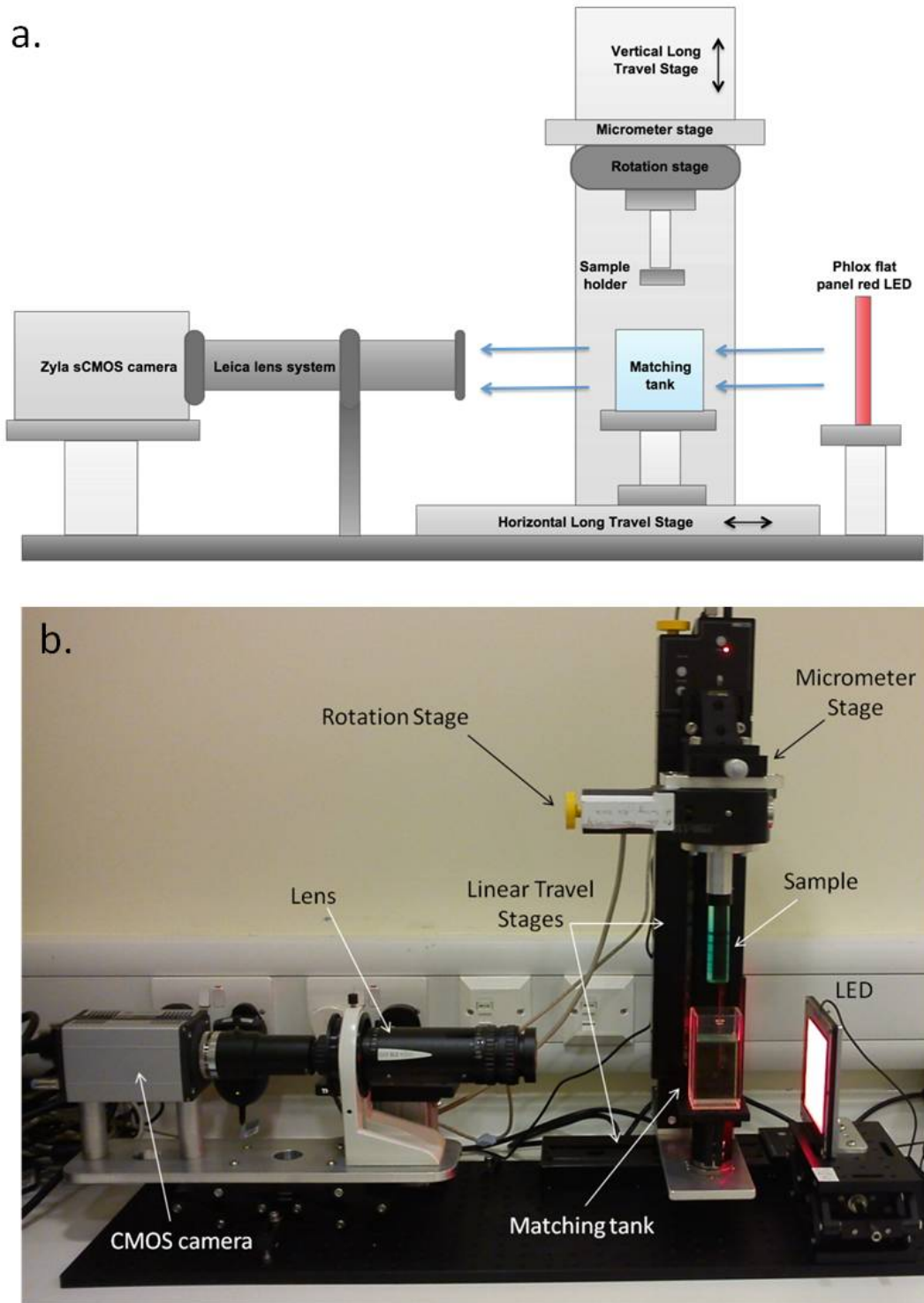**Figure 2.1.** a. *Diagram of the current set-up of optical CT system for dosimetry imaging at the ICR with principal parts of apparatus labelled. b. a picture of the system with PRESAGE® attached.*
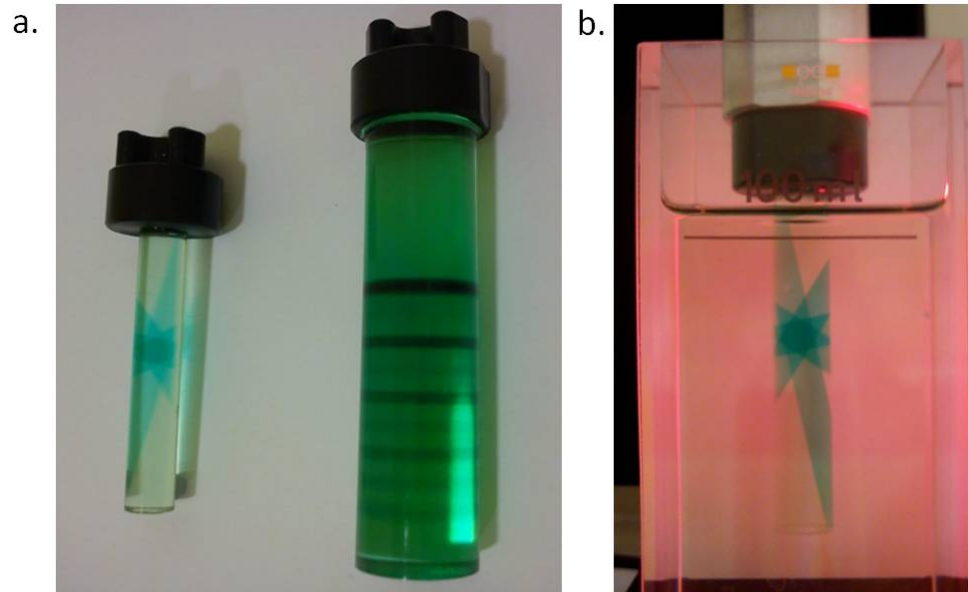
Figure 2.2. *a. PRESAGE® samples with novel 'cap' mounts developed by the ICR workshop. b. A PRESAGE® sample mounted to the rotation stage in the matching tank.*
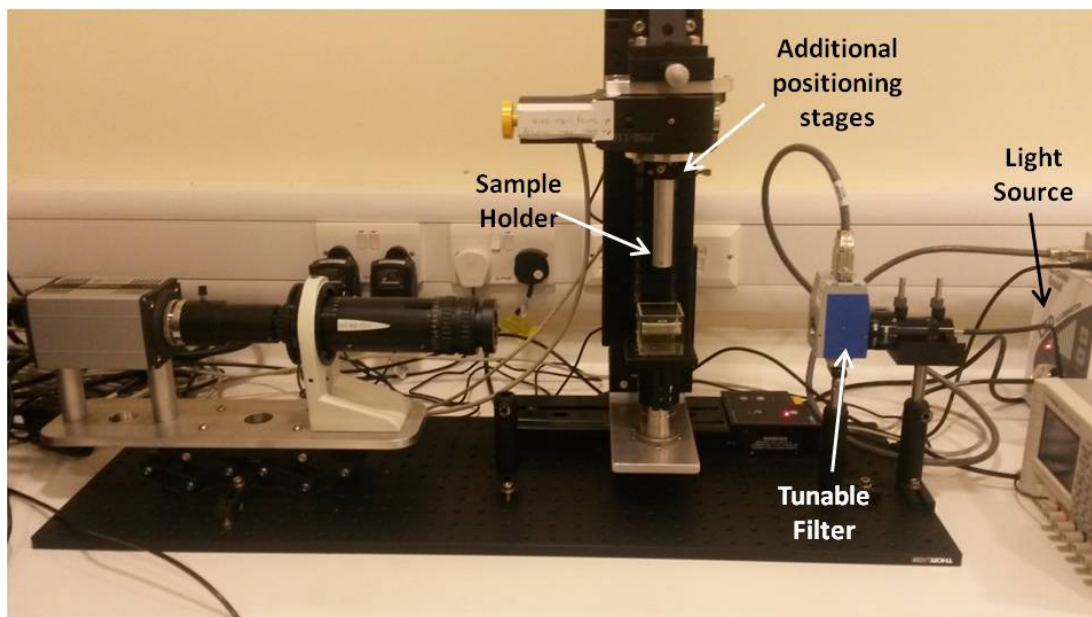

Figure 2.3. *Tissue setup [Need to add more detail on tissue mount]*

2.1.2 Software

2.1.2.1 Acquisition

Image acquisition and sample rotation are controlled synchronously by PC using an in-house program written in LabView (National Instruments Corporation Ltd., Berkshire, UK). The high memory capacities of the PC and camera allow for fast read-out of images, giving much reduced scan times compared to others previously reported.

Projections can be acquired in two modes. Fast scans are performed in 'Continuous' mode, with the sample rotating through 180° at constant velocity and the camera acquiring projections at a fixed frame rate. This method of scanning is only possible because of the large RAM on the computer.

If averaging of several projections is necessary to improve the signal-to-noise ratio (SNR) then a 'Step and shoot' procedure is used in which the sample is rotated by a fixed angle, several images are acquired, averaged and saved before the sample is rotated again. This scan takes much longer however may be necessary in cases where on-camera binning is not used.

'Dark' field (DF) and 'light' field (LF) images are acquired for each scan, to correct for structural noise in the camera and non-uniformities in the light path respectively. In general 30 DF (with cap on camera) and LF (no sample present) images are averaged.

2.1.2.2 Reconstruction

Reconstruction is carried out via Filtered Back-projection (FBP) incorporating 'correction scans', using in-house software written by SJD in IDL (Excelis Visual Information Solutions, Boulder, CO) (see [Doran et al., 2013b]). LF and DF corrections are applied during reconstruction according to equation (4) of [Krstajić and Doran, 2007]. The software allows for manual correction of off-axis COR, which is very difficult to exactly align with sub-pixel accuracy. A ring artefact correction has been added to the reconstruction, based on [Rivers and Gualda, 2009]. Ring artefacts arise from the presence of a defect in the projections which is constant for all angles.

2.1.3 Scanning procedure

[May put this in an Appendix if too much detail for here?]

Before optical scanning of each sample these preparation steps must be followed :

- The rotation stage and matching tank, filled with matching liquid with appropriate RI, are positioned in the centre of the focal plane, using the optical axis LTS positioning stage (see Section 2.2.3).

- The sample is attached to the rotation stage via a sample holder 'cap' and lowered into the matching tank using the vertical LTS translation stage.

- The magnification is chosen such that the widest part of the sample fits within the camera field-of-view (FOV).

- The projection image matrix size is chosen depending on the required resolution of the final images. Larger matrix projections take longer to acquire and reconstruct. On-camera binning is available which improves SNR of projection images and gives smaller matrix projections covering the entire FOV.

- The depth-of-field (DOF) can be adjusted using an aperture in the lens system. The aperture setting will depend on the desired DOF and resolution trade-off (see Section 2.2.2).

- The light-source intensity is adjusted, avoiding saturation of the light-field correction images. This intensity will depend on the magnification, camera binning and aperture settings.

- Before image acquisition, the alignment of the COR with the centre of the FOV can be corrected using a LabView program which compares projections at $0°$ and $180°$. Off-centre COR leads to artefacts which can be corrected as part of the reconstruction.

- Once the COR is correct, samples using the tissue mount, with additional micrometer positioning stages, can be positioned in the middle of the FOV.

- The number of projections depends on the projection matrix size and is calculated using the Nyquist sampling condition,

$$N_{proj} = \frac{\pi}{2} N_{pix} \tag{2.1}$$

where N_{proj} is the number of projections and N_{pix} is the number of projection matrix pixels in the plane orthogonal to the vertical axis.

- Projections are then acquired in either 'Continuous' or 'Step-and-shoot' mode, depending on application. Light and dark field images are acquired afterwards

with identical imaging parameters.

- Reconstructed images are produced using IDL software.

2.1.4 Tissue sample preparation

Ex vivo tissue samples ranging in size from tumour spheroids (roughly 100 μm) to entire rodent organs and tumours (up to 2.5 cm) can be imaged using optical CT. A process of optical clearing is required before imaging to reduce optical attenuation, allowing some photons to pass through the sample to form a projection image. Clearing reduces light attenuation due to scattering, so any contrast is due to natural differences in light absorption properties between different tissue types. Highly attenuating areas, such as haemoglobin in the heart, or lipid-dense areas of the brain, appear bright in reconstructed optical CT images. Some examples of cleared tissues are shown in Figure 2.4. The most commonly used clearing method in this work used benzyl benzoate:benzyl alcohol (BABB) as a clearing agent. After dissection of the tissue, the clearing and preparation process is as follows:

- The tissue is fixed in 70% ethanol in phosphate-buffered saline (PBS) overnight.

- Embedded in 0.75% agarose for stability.

- 3–4 washes of 100% ethanol.

- Washes of 30% and 70% 1:2 benzyl benzoate:benzyl alcohol (BABB) in ethanol.

- 1–2 washes of 100% 1:2 BABB (refractive index 1.559).

- Superglue agarose to sample holder prior to imaging with 1:2 BABB matching fluid.
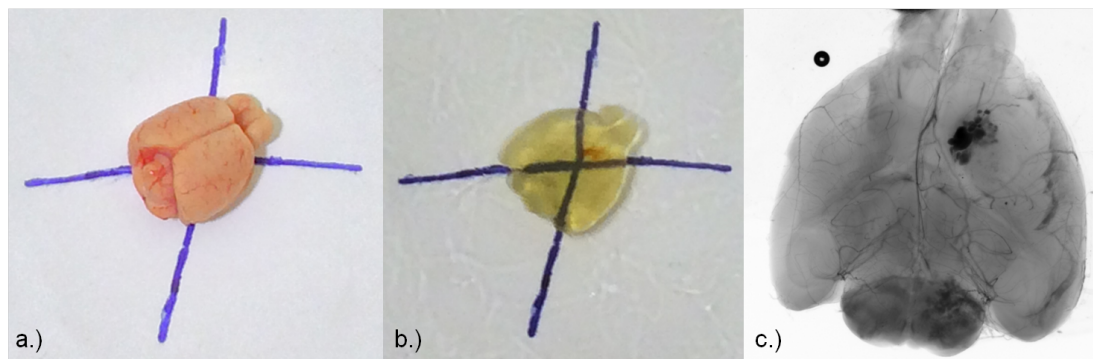

Figure 2.4. *a. Example of an uncleared mouse brain, b. a cleared mouse brain in 1:2 BABB solution, c. a projection image of the cleared brain mounted in the optical CT system. [May take some higher quality pictures of a couple of organs]*

2.2 Optical CT system characterisation

2.2.1 Linear response

In order to establish the relationship between optical CT reconstructed pixel value and optical absorbance, gel finger phantoms were made in a similar fashion to [Oldham et al., 2003].

A specialised finger phantom mould was made by the ICR workshop. A 3-D printed plastic mould contained three removable metal rods on one side and an attachment for the rotation stage on the other. Cylindrical pieces of Teflon FEP sleeving (RI 1.341, Holscot Fluoroplastics Limited, Grantham, UK) were cut a length of 4 cm, the height of the matching tank and one end was heat shrunk onto the plastic mould providing a secure support for the cooling gelatin. A small gap between the Teflon sleeve and the mould was left to allow airflow, meaning the metal rods can be removed easily.

Clear gelatin (10% porcine gelatin (G2500, Sigma-Aldrich) in water) was allowed to set at room temperature around the metal rods, which were then carefully removed. Evans Blue (T-1824), an azo dye which is both optically absorbing and fluorescent, was used to provide optical contrast. Small amounts of Evans blue were added progressively to gelatin which was kept at 30°C using a heater-stirrer. The Evans blue-doped gelatin was injected into inclusions left by the metal rods using a 1 ml syringe. A cuvette of each concentration of Evans blue gelatin was filled and allowed to set. The optical absorbance of each cuvette was measured using a spectrophotometer. Two phantoms were made in this manner, phantom A had 3 mm diameter inclusions and phantom B had 2 mm inclusions, with increasing Evans Blue concentrations.

The phantoms were scanned under the same imaging conditions. The matching liquid used was 4.5% salt solution (RI $\approx$ 1.341) which gives a closer refractive index match to Teflon FEP than water. The average reconstructed pixel value of each finger was calculated from a single axial slice and averaged over a 25×25 pixel area within the inclusion (see Figure 2.5b). As can be seen in Figure 2.5c, the reconstructed pixel value of the optical CT system is linearly related to the optical absorbance as measured by spectrophotometer. The use of two phantoms verifies the linear relationship and the repeatability of measurements.
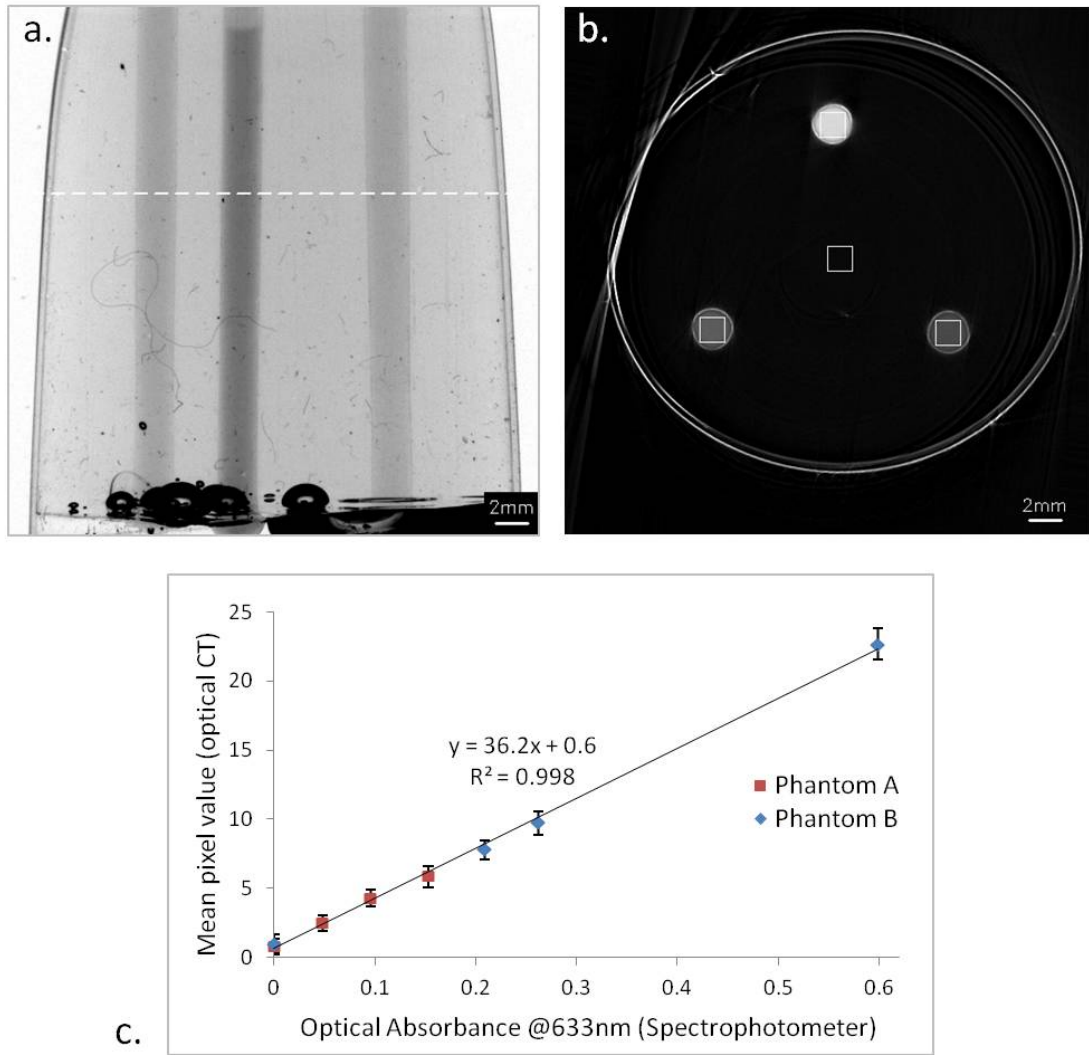
Figure 2.5. *a. An optical CT projection image of a gelatin phantom containing 'finger' inclusions of different concentrations of Evans blue-dyed gel. b. A reconstructed slice through the phantom in the axial position marked by the dashed line in (a). Regions of Interest (ROIs) mark where the mean pixel value was calculated for each finger and the clear gelatin. The double ring artefact is due to refractive index mismatch between gel and the Teflon FEP container, and also between the Teflon and 4.5% saline matching liquid. c. Plot of absorbance of Evans Blue-doped gel measured with a Spectrophotometer against mean pixel value of different regions on reconstructed optical CT images. Two phantoms were measured with all variables constant between readings.*

2.2.2 Spatial resolution

Understanding the spatial resolution response of the optical CT system is very important for acquiring high-quality, quantitative images. There are many factors which can

affect optical CT resolution (see theory section?). Previous publications noted a reduction of optical CT image contrast of small features as the feature size approaches the resolution. [Doran et al., 2013a] This effect is evident even when the feature size is several times the nominal spatial resolution and leads to non-linear response to optical absorbance. Therefore, the limits of spatial resolution of the system must be carefully characterised before we can be confident that measurements are quantitative.

For optical CT the spatial resolution either side of the focal plane along the optical axis is important. The distance over which the focus is 'acceptable' is known as the depth-of-field (DOF). Ideally the DOF of projection images should be larger than or equal to the sample size, as demonstrated in Figure 2.6. However, there is a trade-off between DOF and spatial resolution, Δx, given by [Inoué and Spring, 1997b] as follows,

$$\text{DOF} = \frac{n_{bath}}{0.61n\lambda}\left(\Delta x^2 + \frac{ne}{M_{\text{lat}}}\Delta x\right) \tag{2.2}$$

where n_{bath} is the refractive index of the medium surrounding the sample, n is the refractive index of the medium around the lens, λ is the wavelength of light, e is the pixel size of the camera and M_{lat} is the lateral magnification of the system. The DOF of the system can be adjusted by adjusting an aperture in the lens system. This adjusts the overall acceptance angle of the system, θ, which in turn controls the numerical aperture (NA), which is inversely proportional to the resolution and DOF.

$$\text{NA} = n\sin\theta = \frac{0.61n\lambda}{\Delta x} \tag{2.3}$$
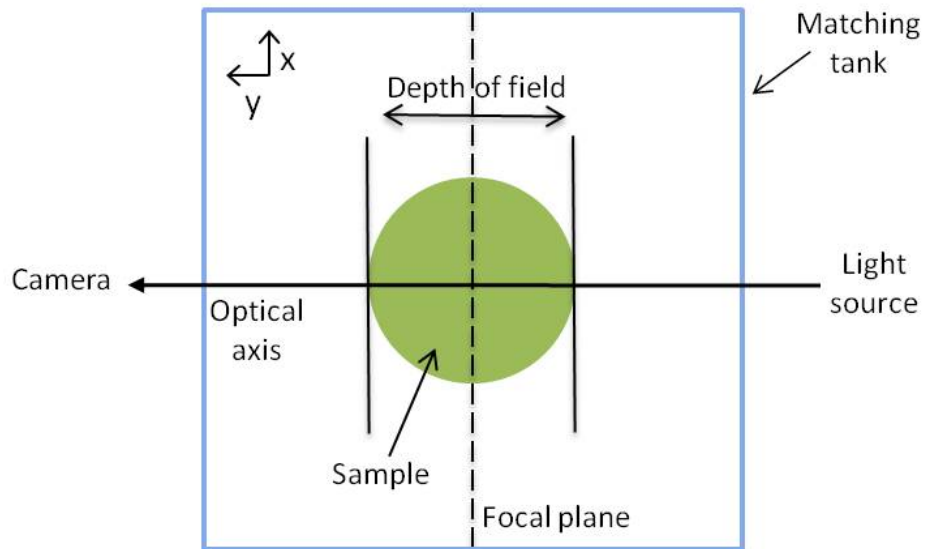

Figure 2.6. *Schematic of the optical CT system geometry showing the ideal positions of the focal plane and depth-of-field.*

To investigate the effect of changing the NA of our system we measured the modulation transfer function (MTF) for a range of positions along the optical axis. Five different NA values were evaluated, corresponding to the five reproducible aperture size settings on the lens system, labelled as A1 to A5, with A1 being the smallest aperture and A5 being the fully open aperture setting, with the largest NA.

The modulation transfer function (MTF) characterises the resolution of a system by measuring how different spatial frequencies are transmitted. It is the Fourier transform of the Point Spread Function (PSF), giving a more comprehensive description of an optical system than quoting a single resolution value. There are various methods of measuring the MTF, including simulating a point source or measuring the response to a sinusoidal pattern. These methods require test objects accurate to sub-pixel distances. It is much easier to manufacture an accurate sharp edge rather than a point source or slit. It has been shown that the MTF can be calculated analytically from the Edge Spread Function (ESF) as follows,

$$\text{MTF}(f) = \mathscr{F}\left[\text{LSF}(x)\right] = \mathscr{F}\left[\frac{d}{dx}\text{ESF}(x)\right] \tag{2.4}$$

where f is spatial frequency, x is displacement and LSF is the Line Spread Function given by the profile of a slit source. [Boone et al., 1986]

A knife edge was positioned at the focal plane and 50 projection images of matrix size 2048×2048, FOV 10×10 mm, were acquired and averaged to improve the signal-to-noise ratio (SNR). The knife edge was moved in steps of 0.1 mm away from the focal plane in both directions along the optical axis. Images were acquired over a distance of 5 mm in each direction giving a total distance of 10 mm, the same as the FOV of each projection image. This was repeated for each aperture setting of the microscope lens.

The MTF was calculated from the ESF, measured across the centre of the knife-edge images, according to equation 2.4 for each position along the optical axis and for each NA value. A comparison of the MTF at the focal plane, 1 mm and 2 mm away from the focal plane for an aperture setting of A3 is shown in Figure 2.7. The 10% MTF value indicates the highest frequency that can be resolved by the system. From Figure 2.7, it can be seen that the 10% limiting frequency gets smaller with distance from the focal plane.

In Figure 2.8 the MTF is represented by a grey level in a 2-D image in which the horizontal coordinate corresponds to spatial frequency, up to 100 mm^{-1} (equivalent to a 10 µm line-pair), and the vertical coordinate corresponds to position along the optical axis. This allows visualisation of the DOF for each of the different NA values.

The maximum resolution and corresponding DOF were measured for each NA setting. The maximum resolution was defined as the largest spatial frequency with an MTF above 10% at the focal plane. The DOF for this frequency was defined as the distance along the optical axis for which this spatial frequency had an MTF above 10%. The observed DOF and resolution results are shown in Table 2.1. It is apparent that for low NA, there is a constant, low resolution across the entire FOV whereas at high NA there is a small region of high-resolution with other areas being defocused.
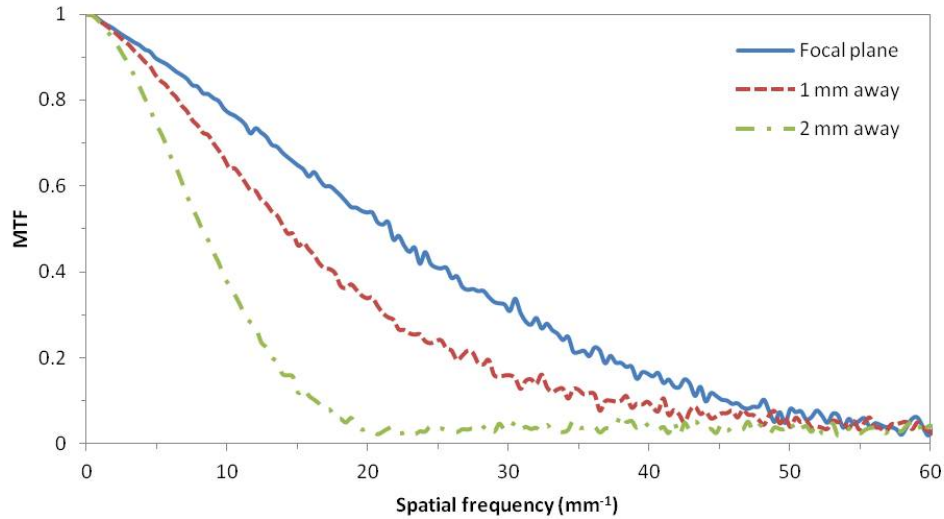
Figure 2.7. *The MTF is plotted against spatial frequency for an aperture setting of A3 for three positions along the optical axis. The 10% MTF resolution limit frequency decreases with distance from the focal plane.*

These results indicate that aperture settings must be chosen carefully for each imaging application. For most cases a constant resolution across the FOV is desirable, therefore A1 is appropriate. For some cases, it may be desirable to have very high resolution in a small area around the centre of rotation in which case a higher aperture setting may be appropriate. These measurements were all taken in 'projection' space and do not take into account the effect of the reconstruction process on resolution.
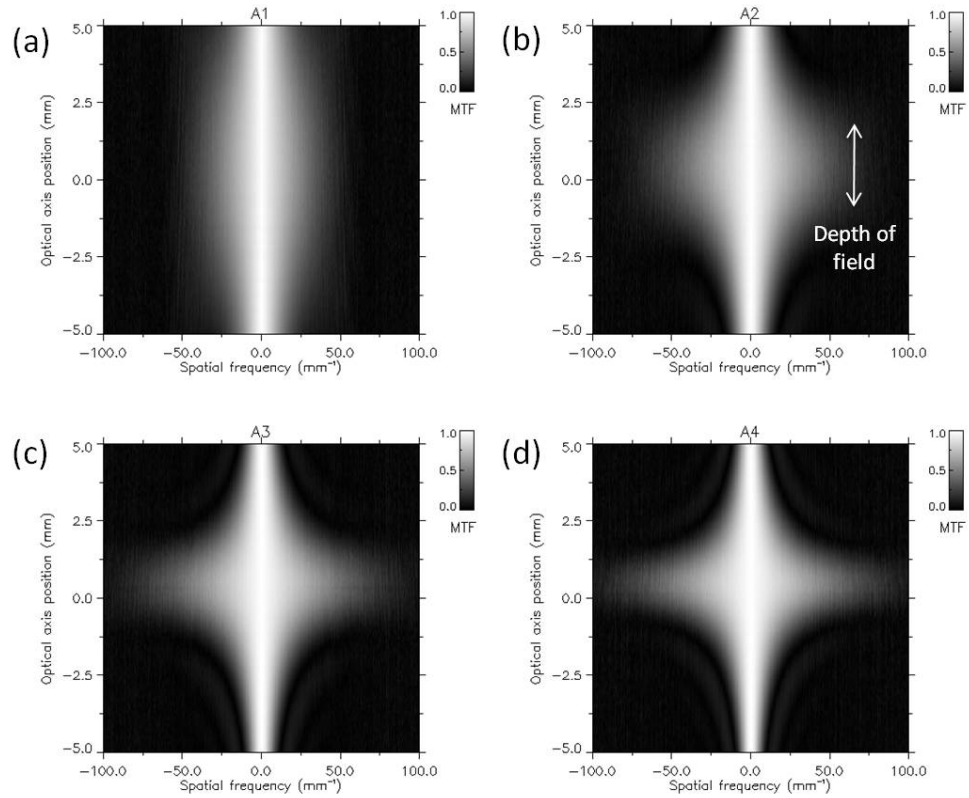
Figure 2.8. *Measurements of the modulation transfer function (MTF) along the optical axis for different numerical aperture (NA) settings of the system, (a) A1 (b) A2 (c) A3 (d) A4. This allows visualisation of the depth-of-field (DOF).*

NA setting	NA	Resolution (μm)	Depth of field (mm)
A1	0.0086	21.5 ± 0.5	9.3 ± 0.4
A2	0.0155	13.7 ± 0.1	2.4 ± 0.2
A3	0.0204	12.0 ± 0.2	1.6 ± 0.2
A4	0.0252	10.1 ± 0.2	0.6 ± 0.1
A5	0.0290	9.7 ± 0.2	0.4 ± 0.1

Table 2.1. *Maximum resolution and corresponding depth-of-fields for different NA settings on the optical CT system. The uncertainties reflect noise in the modulation transfer function (MTF) measurements.*

2.2.3 Focal position

Positioning the COR exactly at the focal plane is important for even focus across samples and can be difficult to achieve. The COR can be moved repeatably through the use of a motorised positioning stage. A method to visualise the defocus caused by mis-
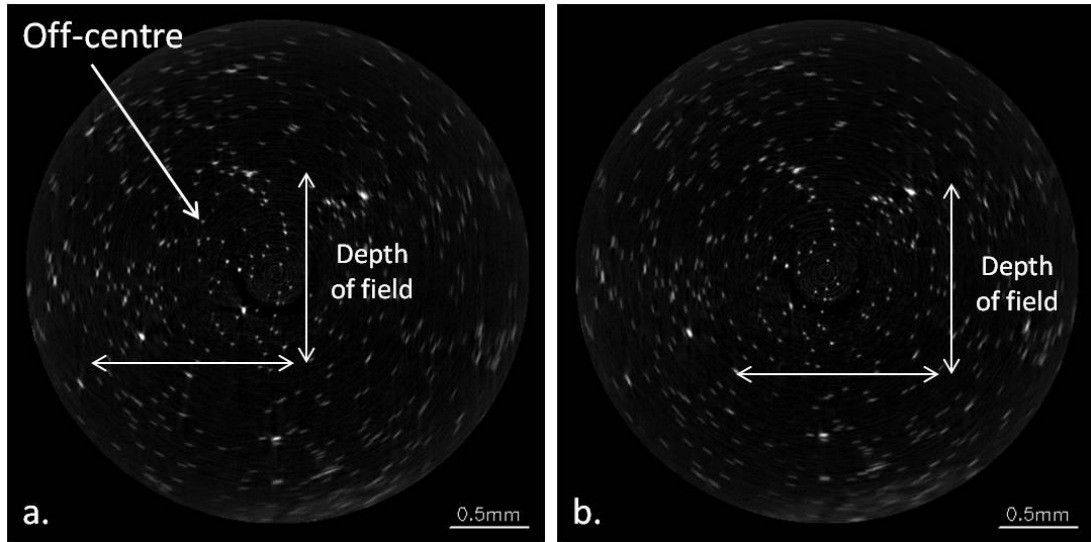
Figure 2.9. *a. Summation of 50 slices of a 'point' object bead phantom, where the centre of rotation (COR) was 0.2 mm away from the focal plane, showing unsymmetrical focus. b. Similar image with the with the COR position correctly aligned with focal plane, showing focus symmetric about the centre of the image.*

alignment of the COR was developed to help focus the system and find the optimum position for the motorised stage. A phantom containing 'point' objects was constructed of 1 μm diameter beads (56314, Sigma-Aldrich) suspended in 0.75% agarose gel. The gel was scanned under 'Continuous' mode with aperture setting A5 (smallest DOF) and reconstructed voxel size $(6.5 \text{ μm})^3$, for a range of positions of along the optical axis.

In order to visualise the defocus over the entire sample cross-section, 50 reconstructed slices were summed together, seen in Figure 2.9 for two positions of the COR. This gives excellent visualisation of the depth-of-field as beads suspended in the gel appear extended and less intense when out-of-focus. When the COR is misaligned with the focal plane, the centre of the DOF is shifted away from the centre of the image due to the 180° rotation. The COR position along the optical axis was incremented until the centre of the DOF was found to be in the centre of the image. This COR position along the optical axis was used for all future experiments. It is also possible to attach this bead phantom to the bottom of other samples which, giving the ability to quantify how the resolution changes over the FOV.

2.3 Conclusions

During the course of this project the optical CT system has been developed and improved over previous systems. The speed of acquisition was significantly improved with a new acquisition protocol and hardware. Adaptations to allow tissue imaging have been made and a tissue sample preparation process has been established.

The system has been thoroughly characterised, which is important before quantitative measurements can be made. Linearity of optical absorbance response has been established and the spatial resolution characterised for different NA settings. These results will be used to help make informed choices on the optimal scanning parameters for future samples.

3 Dosimetry for Microbeam Radiation Therapy

3.1 Introduction

3.1.1 Introduction to MRT

Synchrotron microbeam radiation therapy (MRT) is an advanced form of external beam radiotherapy treatment. It exploits the remarkable tolerance healthy tissue has for high doses of radiation when the doses are 'spatially fractionated', that is, confined to a set of spatially separated regions, each of very small volume. The effects of such radiation are strongly dependent on the geometry of the regions exposed and, in particular, on the width of the incident beam of radiation [Bräuer-Krisch et al., 2010]. It is hypothesised that although normal tissue in the beam path is destroyed, regeneration of blood vessels across the ablated region is possible providing the beam width is sufficiently small and the 'valley dose' sufficiently low. By contrast, tumour microvasculature seems less able to repair the damage caused.

The molecular mechanisms of this selective radiovulnerability remain under investigation. Pre-clinical studies have investigated healthy tissue recovery after MRT irradiation. For example, a piglet survived for 15 months after MRT irradiation of the brain, showing similar development to the rest of its litter (see Figure 3.1a). Evidence of vessel repair across ablated areas has been observed in chick-embryo chorio-amniotic (CAM) membranes (Figure 3.1b).

3.1.1.1 Technical Challenges

The European Synchrotron Radiation Facility (ESRF) in Grenoble, France is pioneering MRT technology on the ID17 Biomedical beamline. Microbeam therapy must be delivered rapidly, in highly collimated beams to avoid spatial blurring of the beam due to patient movement. For this reason, the high-dose rates and minimal beam di-
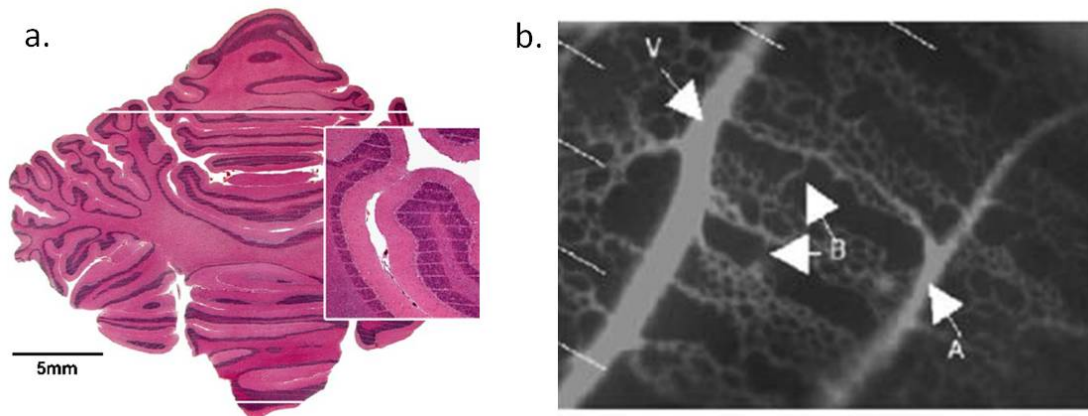
Figure 3.1. a. *Horizontal section of the cerebellum of a piglet of 15 months after irradiation. Although some cells in the path of the microbeam were destroyed, there is no sign of tissue destruction or haemorrhage. (Adapted from [Laissue et al., 2001].) b. chick-embryo chorio-amniotic (CAM) 24 hours after irradiation, white lines mark the locations of microbeam planes. A vein (v), artery (a) and bridge (b) forming across the ablated area are marked.(Adapted from [Blattmann et al., 2005].) Both irradiations had a skin entrance dose of 300 Gy, beam width 27 µm and beam separation 210 µm.*

vergence of synchrotron radiation is ideal for MRT. Relatively low x-ray energies are used (20–100 keV) meaning penetration depth is limited and skin entrance doses are relatively large [Blattmann et al., 2005]. The healthy tissue-sparing geometry of MRT delivery compensates for this.

MRT treatments are usually delivered as an array of highly collimated microplanar beams using a multi-slit collimator (MSC) [Bräuer-Krisch et al., 2005a]. The narrow microbeams (typically 50–100 µm) have large peak entrance doses, commonly over 100 Gy. The valley dose is made up of scattered radiation from surrounding beams and depends on the widths of the peak and valley areas, the depth and the total number of beams. The width of the valley area, the centre-to-centre (ctc) distance, is typically four times the width of the beam.

The geometry of irradiation has been shown to be important to the healthy tissue recovery. The valley dose must be sufficiently small and ctc distance sufficiently wide to allow repair of ablated regions in the peak area. However, to achieve good tumour control it is important to ablate enough tumour. Optimisation of MRT parameters is currently under way in a pre-clinical trial which is also assessing methods for treatment planning and accurate dosimetry for MRT. [REF]

Commercial dosimetry systems are not appropriate for MRT. The small width of the microbeams means that traditional radiotherapy measurement devices (ion chambers,

diode arrays, etc.) are inadequate and many dosimeters cannot withstand the high dose rates involved. An ideal dosimeter for MRT would have micron-scale spatial resolution with a dynamic range of the order of 10,000.

There are two competing measurement problems in modern MRT, which make it extremely challenging to devise a single technique for treatment verification and quality assurance (QA). Firstly, there is the need to characterise the individual microbeams and make accurate measurements of the peak-to-valley dose ratio (PVDR). The PVDR gives an indication of how safe and effective a treatment will be. A high PVDR, with a large peak dose and small valley between beams is desirable and this metric depends on many factors including field size and depth.

The second problem is that, as MRT becomes increasingly sophisticated, there will be a need to provide high-quality 3-D dosimetry over the entire treated volume. Like conventional radiotherapy, MRT has developed complex delivery geometries including multi-port cross-firing [Bräuer-Krisch et al., 2005b] and interlacing [Bräuer-Krisch et al., 2013, Serduc et al., 2009, Serduc et al., 2010] (see Figure 3.2) in order to increase the dose at the tumour site, while sparing normal tissue. However, given the very small sizes of the beams in the case of MRT, a geometrical error of tens of microns could lead to significant under- or over-dosing. Therefore, the delivery systems need to be accurate to sub-micron levels to avoid errors. Any uncertainty could complicate the interpretation of biological outcomes and may delay or limit clinical uptake, particularly in the paediatric patient populations for whom it could be especially suitable [Laissue et al., 2001].

It is the second requirement that we address in the current work. A dosimeter is needed that can follow the entire 'patient journey', with multiple repositioning steps, from the initial x-ray CT scan, through planning with the newly developed treatment planning system (TPS) to the final treatment.

3.1.1.2 Dosimetry for MRT

As described by [Bräuer-Krisch et al., 2010], there is a long history of investigating different techniques to obtain accurate dosimetry in this challenging situation. The devices evaluated include metal oxide-semiconductor field-effect transistors (MOS-FETs) [Bräuer-Krisch et al., 2003, Siegbahn et al., 2009], fluorescent nuclear track detectors [Akselrod et al., 2006] and silicon strip detectors [Lerch et al., 2011]. Previous studies have used thermoluminescent dosimeter (TLD) [Ptaszkiewicz et al., 2008] and radiochromic film (e.g., [Crosbie et al., 2008, Serduc et al., 2010]) dosimetry to obtain 2-D information. Quantitative comparisons of film dosimetry and Monte Carlo mod-
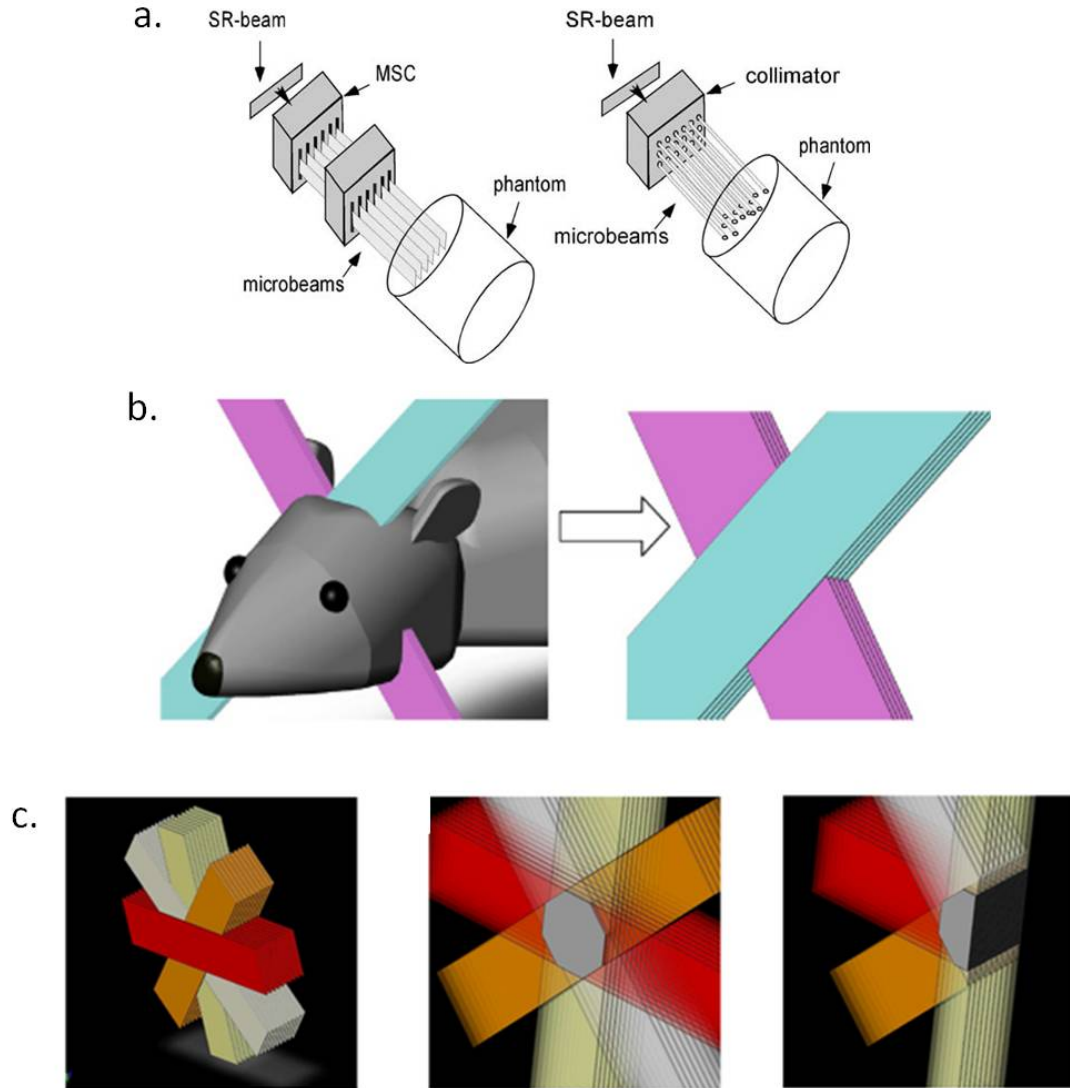
Figure 3.2. *a. Diagrams showing how SR (synchrotron radiation) is formed into either a microplanar array (using a multi-slit collimator (MSC)) or pencil beams (with circular collimators) for MRT treatments. b. Diagram showing the cross-firing irradiation geometry from two ports, with two microplanar fields overlapping in the patient c. Diagram showing a third irradiation geometry, where microbeams are interlaced (rotation and offset) from multiple ports. Images adapted from [Siegbahn et al., 2006], [Bräuer-Krisch et al., 2005b], [Serduc et al., 2010] respectively.*

els have shown good agreement, typically between 2 and 15% depending on the exact measurement location [Martínez-Rovira et al., 2012]. However, whilst film is suitable for some applications (and particularly for the QA of individual fields), 2-D information is of limited use in complex 3-D treatments, such as those presented here. This argument also applies to the direct biological verification of treatment via histological sectioning. Although such work is indispensable for understanding the radiobiological effect of MRT [Crosbie et al., 2010], the quantity of data obtained and spatial coverage are often much more limited. Thus, it is of great interest to develop fully 3-D methods of quantitative, high-resolution dosimetry.

Full 3-D dosimetry of radiosensitive samples has a long history. At the outset, the predominant readout modality was Magnetic Resonance Imaging (MRI) of radiochromic Fricke gels [Appleby et al., 1987, Schreiner, 2004] or polymer gels [Baldock et al., 2010, Maryanski et al., 1993]. The application of MRI dosimetry to MRT was investigated by [Dilmanian et al., 2008] but only for 'thick microbeams' (680 μm) using a commercial scanner. [Berg et al., 2004], [Bayreder et al., 2008] and [Heilemann et al., 2015] have investigated the limits of MRI gel dosimetry for resolving small features, but the minimum width of irradiated region was 200 μm, a factor of four larger than the width of the microplanar beams studied here. The primary limitations for the MRI method are the r^{-3} dependence of image signal-to-noise ratio (SNR) and the diffusion path length of water molecules during each scan step. A further problem is that the gels used cannot always support the high dose rates encountered in synchrotron MRT.

3.1.2 Optical CT micro-dosimetry

Optical CT is an alternative modality for 3-D dosimetry readout. Used for some time as a method of clinical verification in large dosimeters, the potential for optical CT using the radiochromic plastic PRESAGE® dosimeter in small-field imaging of millimetre-sized beams is now a subject of considerable interest [Clift et al., 2010]. It offers the exciting possibility of quantitative 3-D data with microscopic resolution, but over an extended field-of-view (FOV) within a macroscopic object. A recent study [Doran et al., 2013b] performed a baseline assessment of the dosimetric accuracy of a microscopy system but highlighted that further improvements in resolution were necessary. To date, the highest nominal spatial resolution so far reported with PRESAGE® is 78 nm, but those results were obtained using traditional fluorescent microscopy [Annabell et al., 2012] rather than transmission optical CT as here and, so far, only for 1-D patterns of dose deposition. More recently full 3-D imaging of fluorescence in PRESAGE® for MRT was demonstrated using confocal microscopy [Gagliardi et al., 2015]. *[Add some comments on this paper]*

The current work has two aims. Section 3.2: 3-D Visualisation establishes how PRESAGE®️ and optical CT can be used as a QA tool for MRT, fulfilling the 3-D dosimetry information gap. Section 3.3: Quantitative measurements of PVDR, investigates in detail the reduction in contrast seen previously and assesses the extent to which optical CT can be used for PVDR measurement.

3.2 3-D Visualisation

3.2.1 Methods and Materials

3.2.1.1 PRESAGE®️

PRESAGE®️ is a solid, radiochromic 3-D dosimeter consisting of a transparent polyurethane matrix (approximately 90% of the dosimeter by weight), 2% leuco malachite green, and a 4% trihalomethane initiator, with the remainder being a solubilizer for the dye and initiator. [Adamovics and Maryanski, 2003] The optical density of the plastic changes after exposure to radiation making it very useful for monitoring 3-D dose delivery. The PRESAGE®️ formulation used has the stoichiometric chemical formula $C_{304}H_{510}N_{20}O_{71}SBr$, and a mass density of 1.11 gcm^{-3}.

Custom made PRESAGE®️ samples were supplied by the manufacturer (Heuris Pharma, Skillman, NJ) in the form of cylinders of diameter 22 mm and 9.7 mm. The polyurethane leucodye solution was poured into a mould and pressurized at 60 psi for at least 48 hours to ensure a solid dosimeter. These cylinders were machined to a uniform heights of 50 mm for the 9.7 mm diameter samples and 80 mm for the 22 mm diameter samples. During irradiation the samples were inserted into a bespoke Perspex phantom that was used both for holding the samples and to provide adequate scatter conditions for secondary electronic equilibrium [Doran et al., 2013b].

PRESAGE®️ has quite a high RI of around 1.5 which requires specialised matching liquid for imaging. A mix of 2-ethylhexylsalicylate (W514500-10KG-K, Sigma-Aldrich) and 4-methoxycinnamic acid 2-ethylhexylester (Chem. Art. 100255, Chemos GmbH) was made in an 11:1 ratio and then adjusted by trial and error to give a close match [Abdul Rahman et al., 2011b]. To increase the dynamic range an oil-soluble green dye was added to give the liquid a similar absorbance as PRESAGE®️.

The linearity of the PRESAGE®️ dose response was confirmed using cuvettes irradiated with a range of doses. The optical absorbance of each cuvette was measured using a spectrophotometer (see Figure 3.3a&b).

Two PRESAGE® samples were irradiated with a calibration pattern, similar to [Doran et al., 2013b]. The relationship between optical CT pixel value and dose must be established for each batch of PRESAGE®. Figures 3.3c–e show the calibration pattern and the linear dose response.

3.2.1.2 Sample irradiation

Irradiations were carried out at the European Synchrotron Radiation Facility (ESRF) in Grenoble, on the ID17 biomedical beamline. The methodology, equipment and beam characteristics have already been described in detail [Abdul Rahman et al., 2011a, Doran et al., 2013b, Doran et al., 2010b].

Successful delivery of MRT dose patterns is extremely demanding from an engineering point of view. Accurate sample alignment plays a key role and a 3-D dosimeter capable of a simple 'hit-or-miss' assessment is highly desirable. The pattern formed by the 2-D intersection of multiple, angled arrays of microbeams has the potential to be extremely complicated and so the use of a single or small number of 2-D films for QA purposes is not a viable option. Furthermore, performing accurate quantitative measurements of 2-D optical density on multiple films is an extremely time-consuming operation. Having a method of generating information to correct or improve the MRT delivery would be extremely useful. For this purpose, fully quantitative measurements of peak dose would not be required. Instead the main requirements are fast readout, ease of use, spatial accuracy and visualisation of dose integration.

To test whether optical CT is suitable in this capacity, different complex MRT irradiations were performed, listed in Table 3.1. These included collimated beams (pencil beams, sample 1.1) [Bräuer-Krisch et al., 2010], interlacing of microplanar beams (multiport and offset, sample 1.2) [Serduc et al., 2010], multi-port cross-firing of microplanar beams with the use of an anthropomorphic head phantom (sample 1.3, see Figure 3.4) [Requardt et al., 2005]. All beams had a full width half maximum (FWHM) of 50 μm and centre-to-centre (ctc) spacing of 400 μm between beams.

3.2.1.3 Optical CT microscopy

Imaging was performed using the optical CT microscope described in Section 2.1. With the previously reported system it took approximately 1 hour 10 minutes to acquire the data for a 512^3 voxel reconstructed volume. [Doran et al., 2013b] The equivalent scan takes under 3 minutes with the new system, making optical CT a viable system for *in situ* feedback for MRT irradiations. Although, for the results presented here,
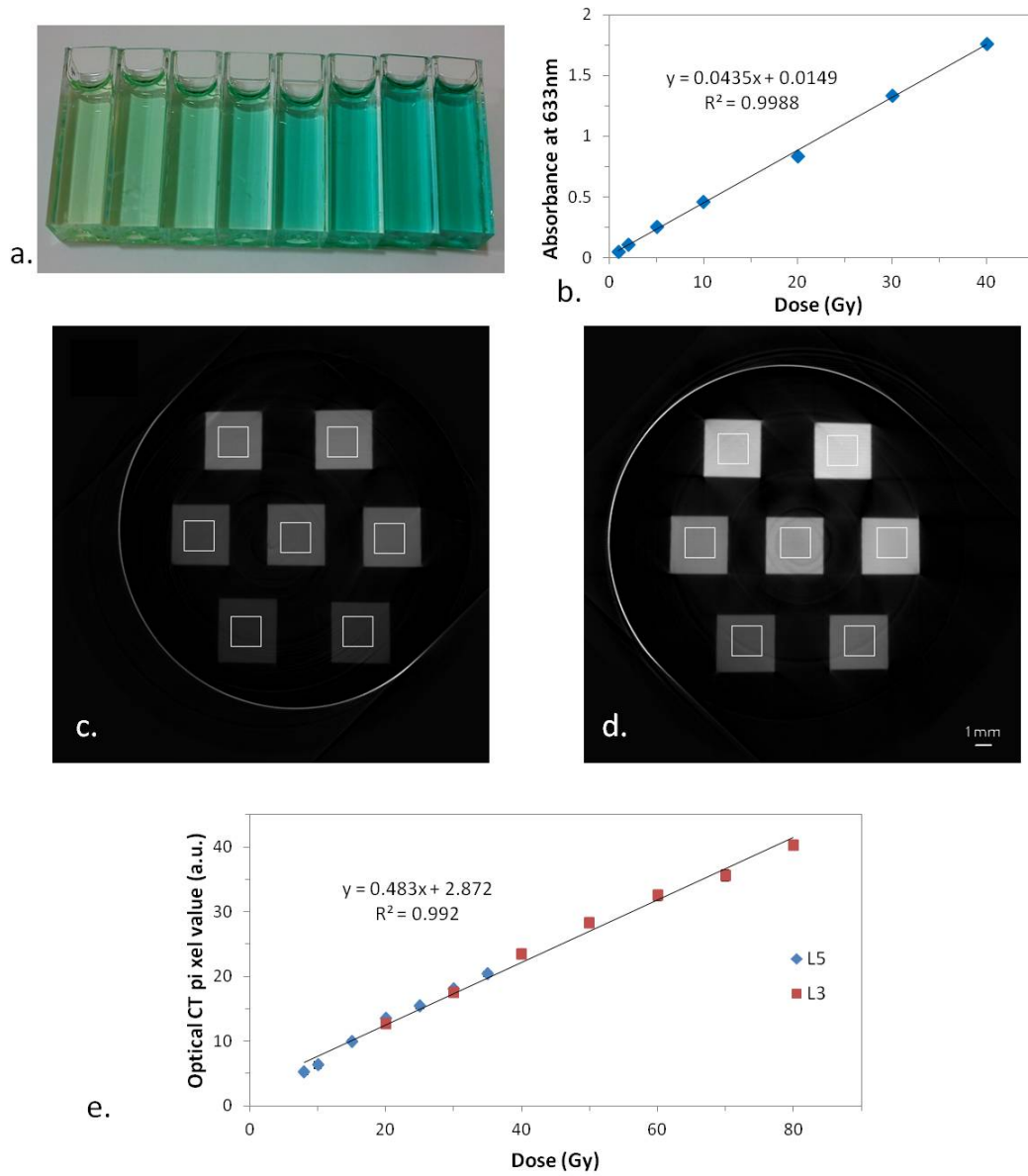
Figure 3.3. *a. Cuvettes of PRESAGE irradiated with the RMH linac with a range of doses, b. the optical absorbance of the cuvettes measured using a spectrophotometer. c. Sample L5 with dose calibration pattern and d. sample L3 with higher doses, both at depth of 0.3 cm e. The calibration curve for the two samples at depth of 0.3 cm.*

Sample	Irradiation type	Peak dose (Gy)	Dosimeter size (mm)	Description
1.1	Pencil beams	300	9.7	Four fields of 7×7 interlaced circularly collimated 'pencil' beams, separated by 45° rotation.
1.2	Interlacing	200	9.7	Four $(5 \times 5)\mathrm{mm}^2$ microplanar arrays separated by 45° rotation and 200 μm offset.
1.3	Multiport cross-firing	200	22	In anthropomorphic head phantom, three $(10 \times 10)\mathrm{mm}^2$ microplanar arrays separated by 60° rotation.
2.1	Single microplanar array	100	9.7	$(10 \times 10)\mathrm{mm}^2$ microplanar array field.
2.2	Single microplanar array	50	9.7	$(10 \times 10)\mathrm{mm}^2$ microplanar array field.
2.3	Single microplanar array	100	9.7	$(30 \times 30)\mathrm{mm}^2$ microplanar array field.

Table 3.1. *List of sample irradiations.*

Scan	Projections	Pixels	Voxel size (μm)	Acquisition time
Fast	1000	512×512	20.8	2.5 minutes
High-resolution	3200	2048×256	5.2	1 hour

Table 3.2. *Different optical CT scanning parameters for MRT dosimetry samples.*

the scanner and irradiation facility were not co-located, there is clear potential for installing an optical CT microscope in the beamline 'hutch' of the accelerator. The new automated positioning system and custom-made sample mounts allows reproducible sample scanning position, making it easy to measure the samples immediately pre- and post-irradiation, thus potentially allowing absolute measurements of optical density change in the future, reducing artefacts and baseline uncertainties.

Two scanning procedures were used for scanning dosimetry samples, detailed in Table 3.2. Samples 1.1-1.3 were scanned using a 'fast' three minute scan of 1000 projections over 180° rotation, each of 512×512 pixels, satisfying the Nyquist condition for the reconstruction of an isotropic data volume of 512^3 voxels. The FOV was $(13.3 \text{ mm})^3$ for the 9.7 mm diameter samples (1.1 and 1.2) and $(26.6 \text{ mm})^3$ for the 22 mm diameter sample (1.3) with isotropic reconstructed voxel sizes of $(26 \text{ μm})^3$ and $(52 \text{ μm})^3$ respectively.
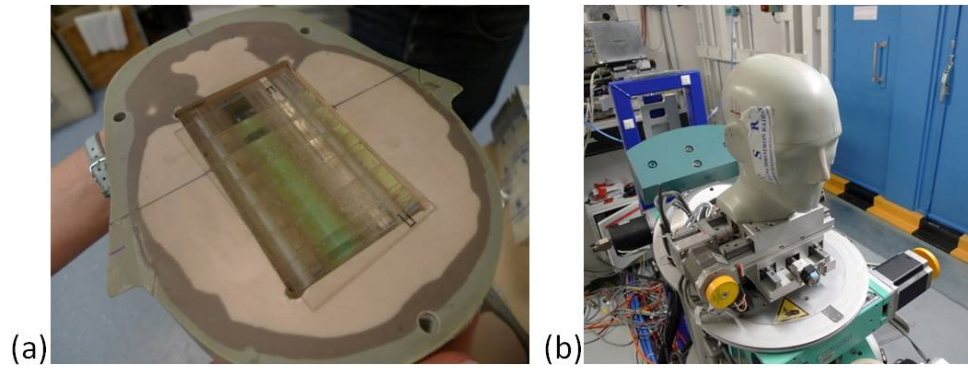
Figure 3.4. *(a) PRESAGE® sample 1.3 in place in anthropomorphic head phantom and (b) the head phantom being positioned for irradiation at the ESRF.*

3.2.2 Visualisation Results

High quality image datasets were acquired for each sample and the microbeams are easily visualised. The reconstructed 3-D datasets can be visualised in different ways to provide an assessment of the irradiation. Figure 3.5 shows a maximum intensity projection (MIP) image of a reconstructed image volume of sample 1.1, with the full dataset available in movie format as online supplementary material. This type of visualisation is very powerful, allowing the user to quickly assess that the pencil beam irradiation has been delivered successfully and is well centred within the sample. Confirming this would be very difficult using 2-D dosimeters.

Figure 3.6 shows a reconstructed slice through sample 1.2, irradiated with an interlaced dose pattern. More views are available in supplementary video material. It is clear that interlacing of the centre and left fields was successful. However, the centre and right fields are overlapping and the increased dose is visualised as a brighter region on optical CT images. This demonstrates the qualitative dose integration visualisation power of optical CT, which would be very helpful during MRT set-up even without a quantitative measure of the increased dose. This visualisation could inform on patient safety and would be complicated to measure with a 2-D dosimeter.

Figure 3.7 shows two orthogonal reconstructed slices through sample 1.3 which was irradiated inside an anthropomorphic head phantom with a multi-port cross-firing geometry. With the ability to choose the image plane arbitrarily, it is easy to find a slice that gives direct interpretation of the delivered dose, unlike the image shown in Figure 3.7(a). The second image, shown in Figure 3.7(b), clearly shows that two of the delivered fields are off-centre and a simple measurement the offset could be used to correct the MRT geometry (red arrow). This interpretation would be very difficult from a 2-D measurement as the 2-D dosimeter would need to be placed very accurately.
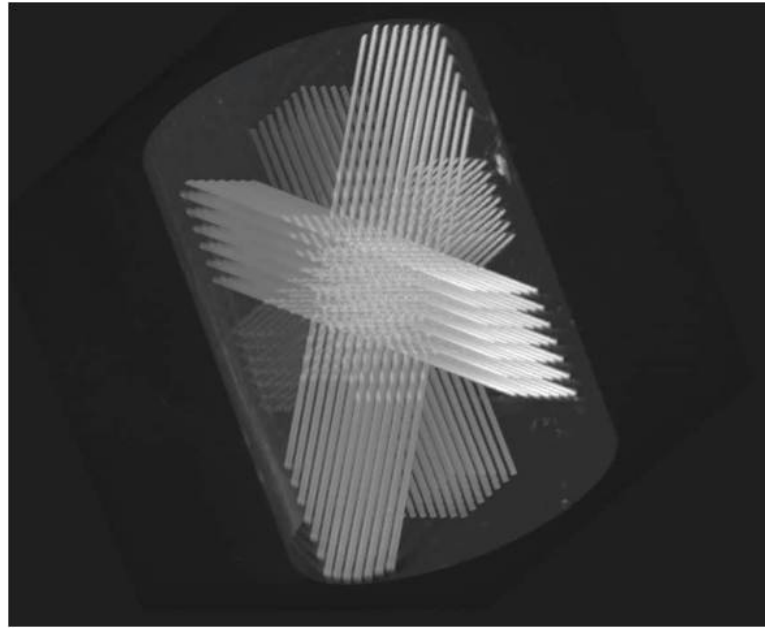
Figure 3.5. *A maximum intensity projection (MIP) image of sample 1.1 showing excellent visualisation of the microbeams, confirming successful irradiation which was well centred within the sample. Full 3-D reconstruction can be seen in a supplementary video.*
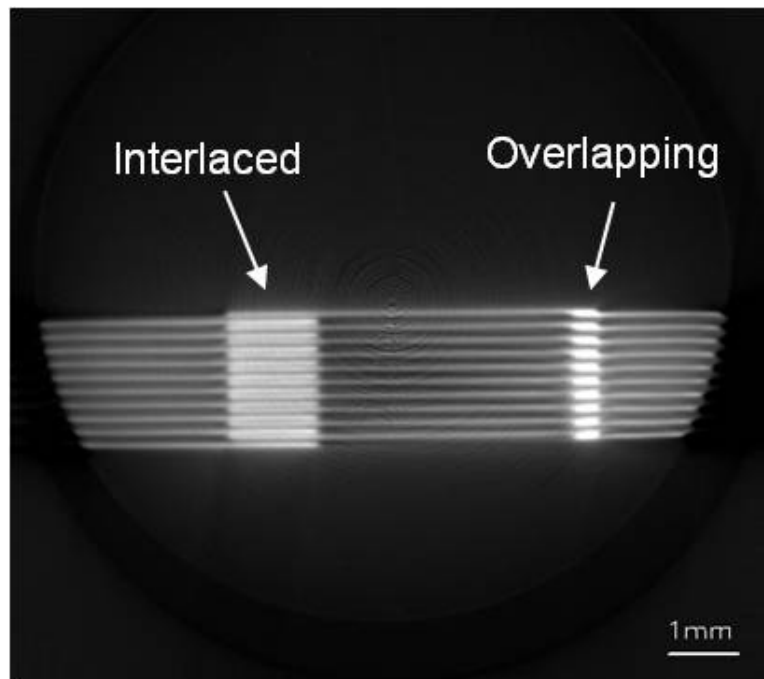
Figure 3.6. *A reconstructed slice through sample 1.2 with an interlaced dose pattern which has overlapped, leading to overdosing compared to the expected treatment. Further slices from the full dataset are available in a supplementary video.*
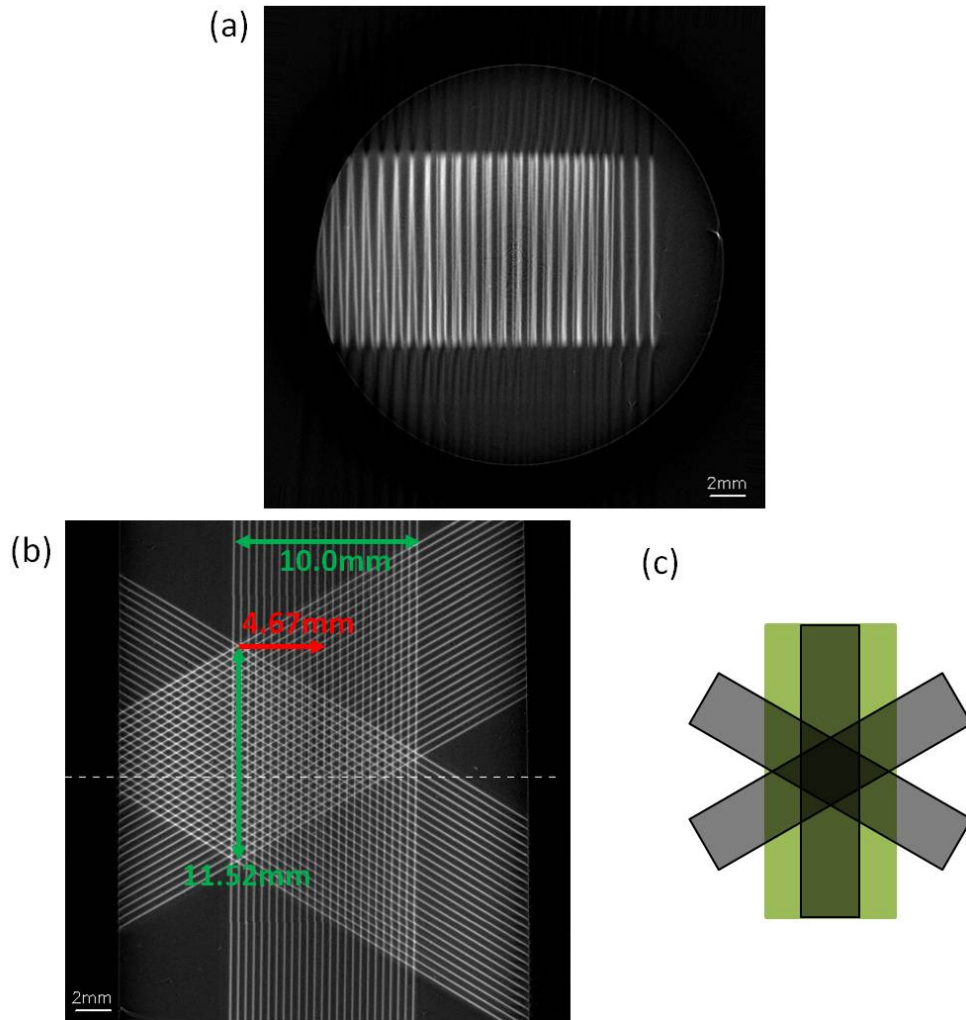
Figure 3.7. *(a) A reconstructed slice through sample 1.3 which was irradiated inside an anthropomorphic head phantom with a multiport cross-firing geometry. From this view it is difficult to tell whether the irradiation was successful. (b) A reconstructed slice in the orthogonal plane, with the z position of (a) marked by the dotted line. Green arrows mark field measurements which are as expected, showing that three irradiations have been delivered at the expected field size and spaced 60° apart as expected. However, two of the fields are offset from the centre of the sample, (c) shows the expected shape of the irradiation. The red arrow denotes the offset of the two incorrect fields from the centre of the sample, this measurement could be used to correct the MRT geometry.*

3.3 Quantitative measurements of PVDR

The peak-to-valley dose ratio (PVDR) is of particular interest to the MRT community, giving a measure of how safe and effective an MRT treatment will be. Measuring this value requires accurate measurement of peak microbeam dose which is very difficult given the small size of the microbeams. A 3-D measurement of PVDR would be extremely useful as it can be used to investigate how this metric changes with depth and with more complex treatments, such as multi-port cross-firing and interlacing.

As previous reports of optical CT micro-dosimetry reported decrease in contrast with small features, it was unclear whether optical CT was capable of measuring PVDR in its current form. [Doran et al., 2013a] These experiments describe an investigation of the limits of optical CT for MRT dosimetry and propose possible improvements for the future.

3.3.1 Sampling investigation

The first task was to determine what sampling pixel size was necessary to measure the peak of a narrow beam. A Monte Carlo generated 50 μm wide microbeam profile (courtesy of E. Siegbahn) was used to simulate a 'sample' irradiated with a microplanar array of microbeams with ctc distance 400 μm. This simulation was used to generate 'projections' which were binned to different matrix sizes to reflect different sampling pixel sizes. The resulting projections were reconstructed using filtered backprojection and the microbeam profiles were compared to the original Monte Carlo profile.

The results shown in Figure 3.8 demonstrate that to measure the peak dose of a 50 μm microbeam with an error of less than 1%, a sampling resolution of 10 μm is required. Therefore, an optical CT pixel size of at least 10 μm is required to measure the PVDR accurately. This simulation is very simple and does not take into account effects such as optical blur.

3.3.2 Optical CT PVDR measurement

PRESAGE® samples were irradiated with microplanar arrays of different field sizes and different peak doses to provide a range of PVDRs for comparison with Monte Carlo and film data. Samples were laid in the phantom and exposed end-on to a single irradiation from a multi-slit collimator of slit width 50 μm, ctc spacing 400 μm [Bräuer-Krisch et al., 2009]. Two 9.7 mm diameter samples were exposed with a nominal peak
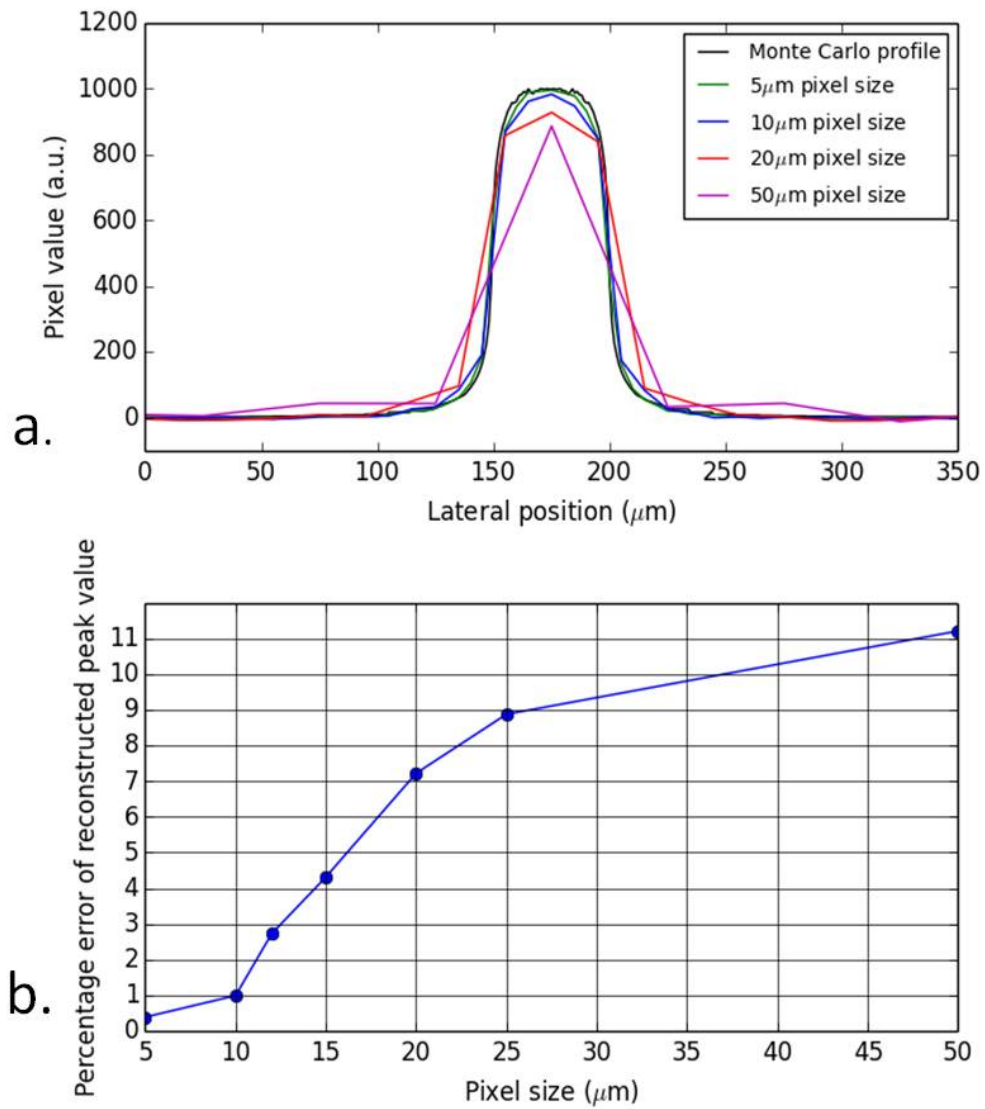
Figure 3.8. a. *Results of a simple simulation, investigating the effects of sampling pixel size on the reconstruction of a Monte Carlo simulated MRT 50* μm *beam profile. b. The percentage error of the reconstructed microbeam peak dose value for each pixel size, compared to the Monte Carlo simulation.*

dose to the surface of the dosimeter of 50 Gy and 100 Gy, both with a field size of (10×10) mm^2 (samples 2.1 and 2.2 respectively). A third 9.7 mm sample was exposed with a nominal peak dose of 100 Gy, with field size (30×30) mm^2 (sample 2.3, see Table 3.1).

Samples 2.1-2.3 were scanned using a 'high-resolution' scan consisting of 3300 projections, each averaged over five acquisitions of 2048×256 pixels, reconstructed to a data volume of $2048 \times 2048 \times 256$ voxels with FOV $(10 \times 10 \times 1.25)$ mm. Using the full matrix size of the new camera across the width of the sample allows significantly higher sampling frequency over previous reports, with an isotropic reconstructed voxel size of $(5.2 \ \mu m)^3$. A smaller matrix height of 256 pixels was chosen for reduced acquisition and reconstruction times. The large computer RAM of 256 GB allows readout of the large amounts of data simultaneously making these scans a manageable 1 hour long. The projections were acquired with the largest DOF setting (smallest NA, setting A1), reflecting the 'ideal' focal situation of constant resolution across the entire sample. The samples were scanned at depths of 0.3 cm, 1 cm and 4 cm for comparison with Monte Carlo and film measurements of PVDR [Martínez-Rovira et al., 2012].

3.3.3 Deconvolution

Using a high NA would give a high resolution at the cost of a small DOF, resulting in out-of-focus data being superimposed on top of in-focus data requiring deconvolution. To investigate whether the resolution could be improved through deconvolution with a measured point-spread-function (PSF), a PSF phantom was designed. The PSF phantom was made using 1 μm diameter beads (56314, Sigma-Aldrich) which were suspended in 0.75% agarose gel. The gel was dehydrated in 100% ethanol and then soaked in matching fluid giving the same refractive index as the PRESAGE®. Superglue was used to attach the bead phantom to the end of PRESAGE® sample 2.1. The bead phantom was then included in the FOV during a 'high-resolution' scan consisting of 3300 projections, each averaged over five acquisitions of 2048×256 pixels, reconstructed to a data volume of $2048 \times 2048 \times 256$ voxels with FOV $(10 \times 10 \times 1.25)$ mm. The lens aperture was set to A4 which had the largest DOF for 10 μm resolution (see Table 2.1).

When images were reconstructed, in principle a bead at point (x, y, z) has experienced the same optical blur as at point $(x, y, z + \Delta z)$. Assuming this, a bead in the centre of the sample in good focus was used as a PSF during Richardson-Lucy deconvolution of the microbeam profile axially above it at a depth of 0.3 cm in PRESAGE®. Deconvolution was performed in the IDL software environment (Exelis Visual Information Solutions,

Boulder, CO) using the 'deconv' tool [Varosi and Landsman, 1993], assuming Poisson noise. The PVDR from the resulting deconvolved profile was calculated for different numbers of deconvolution iterations.

3.3.4 Quantitative Results

3.3.4.1 PVDR measurement

Figures 3.9a&b show a reconstructed optical CT image of PRESAGE® sample 2.1 and the associated profile through the marked position on the image. To reduce noise, profiles were median-averaged in the two orthogonal directions to the microbeam variation resulting in an effective pixel size of 104 µm in those directions and 5.2 µm across the profile. Over this small distance there is no divergence of the peak pixel position in the orthogonal directions as the beam divergence is very small.

As no part of the sample was unirradiated, the baseline corresponding to zero-dose pixel value used is an average of values obtained from unirradiated areas of other samples from the same batch, hence the large uncertainty marked on the graph. In future a pre-scan can reduce this error. As can be seen the sampling frequency is very high, however the beams appear blurred compared to the shape observed with other higher-resolution modalities.

The PVDR was calculated for sample 2.1 at depths of 0.3 cm, 1 cm and 4 cm. Samples 2.2 and 2.3 were also measured at a depth of 4 cm. The results of the optical CT PVDR measurements are plotted against the expected values from Monte Carlo simulation [Martínez-Rovira et al., 2012] in Figure 3.9c, where the large error-bars on the optical CT measurements are principally due to the baseline uncertainty. Encouragingly, the variation of PVDR with depth and field size corresponds extremely well between optical CT and Monte Carlo measurements with a very high correlation coefficient for the linear fit. However, the absolute value of the PVDR, as measured by optical CT is consistently only 30% of the expected value. There could be several reasons for this. Given that decreasing the peak entrance dose has no effect (sample 2.2) it is unlikely to be due to a lack of dynamic range in the optical CT scanner. Sample 2.3 has a larger field size and therefore larger valley dose. Given that this measurement also fits the trend it is unlikely that low SNR in the valley measurement is the primary source of the error.

The full-width half-maximum (FWHM) of one of the beams in Figure 3.9b is 62.4 µm, not 50 µm as expected. This implies that the profile is blurred, which would

reduce the peak value measured. Although the nominal pixel size is 5.2 μm, the true resolution is lower than this, limited by the imaging optics, as expected from our MTF measurements (see Section 2.2.2). Table 2.1 shows that for an aperture setting of A1 the maximum resolution is only 21.5 ± 0.5 μm. A resolution of 10 μm is achieved when the NA is increased at an aperture setting of A4, but in this case, the DOF less than 0.6 mm.

3.3.4.2 Deconvolution

Figure 3.10a shows a microbeam profile and its improved shape after deconvolution with a PSF measured using a 1 μm diameter bead. However, Figure 3.10b clearly demonstrates that although the deconvolution improves the shape of the profile, the PVDR measured is dependent on the number of deconvolution iterations performed, and does not converge before the noise reaches an unacceptable level. This means that this type of deconvolution approach is not reliable enough to use in quantitative measurements of PVDR of microbeams. This may also apply to depth-of-field scanning techniques previously employed in biological imaging to improve the resolution [Fauver et al., 2005a].

3.4 Discussion

Section 3.2 clearly suggests that optical CT has the potential to play an important role in MRT QA. The data of Figures 3.5–3.7, rendered in 3-D in the accompanying movies, demonstrate graphically where the real benefit of the optical CT technique lies. Image data may be acquired from the entirety of the sample at high resolution in a single measurement. This would be very useful for hit-or-miss assessment and imaging is now fast enough to provide correction information to improve MRT irradiations *in situ*. Compared with a single, or small number of 2-D film images, there are no difficulties in interpreting the measured dose distribution in multiport treatments. Using the solid PRESAGE® dosimeter also allows for end-to-end QA of the entire treatment process including CT scan, treatment planning, positioning and delivery which would be necessary before MRT is translated to clinical use. One potential future application would be to combine PRESAGE® dosimetry with a patient motion simulating platform which can investigate whether very complex irradiations such as interlacing are possible with patient breathing motion.

The time between irradiation and readout was longer than desirable, during which time
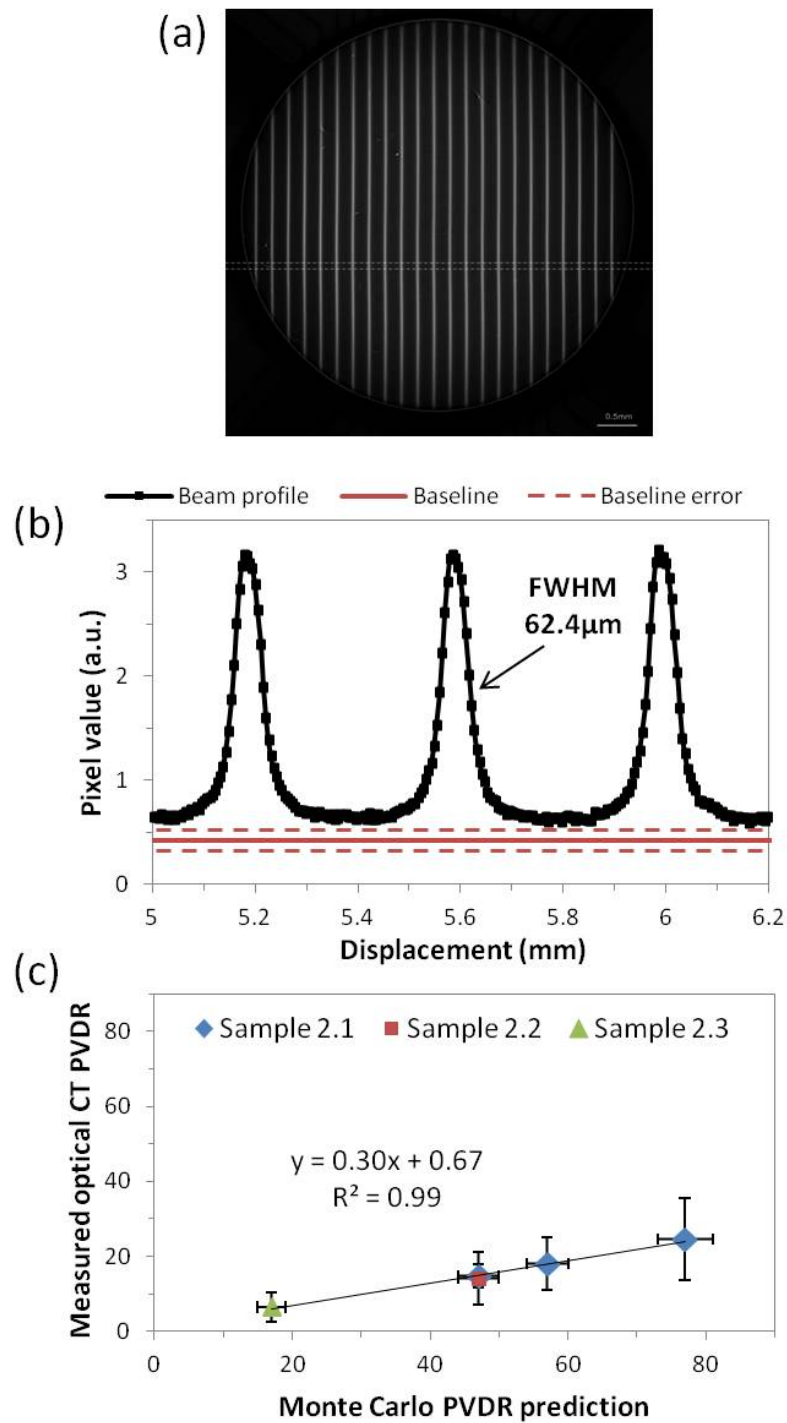
Figure 3.9. *(a) Reconstructed image of sample 2.1 and (b) the corresponding profile through microbeams. The baseline is an average value from unirradiated areas on other samples from the same batch, hence the large uncertainty. The profile was median averaged along 20 pixels in the directions orthogonal to the profile to improve the SNR resulting in 5.2 μm pixel size across the profile and 104 μm pixel size in the orthogonal directions. (c) Comparison of PVDR measurements using optical CT against expected values from Monte Carlo simulation [Martínez-Rovira et al., 2012].*
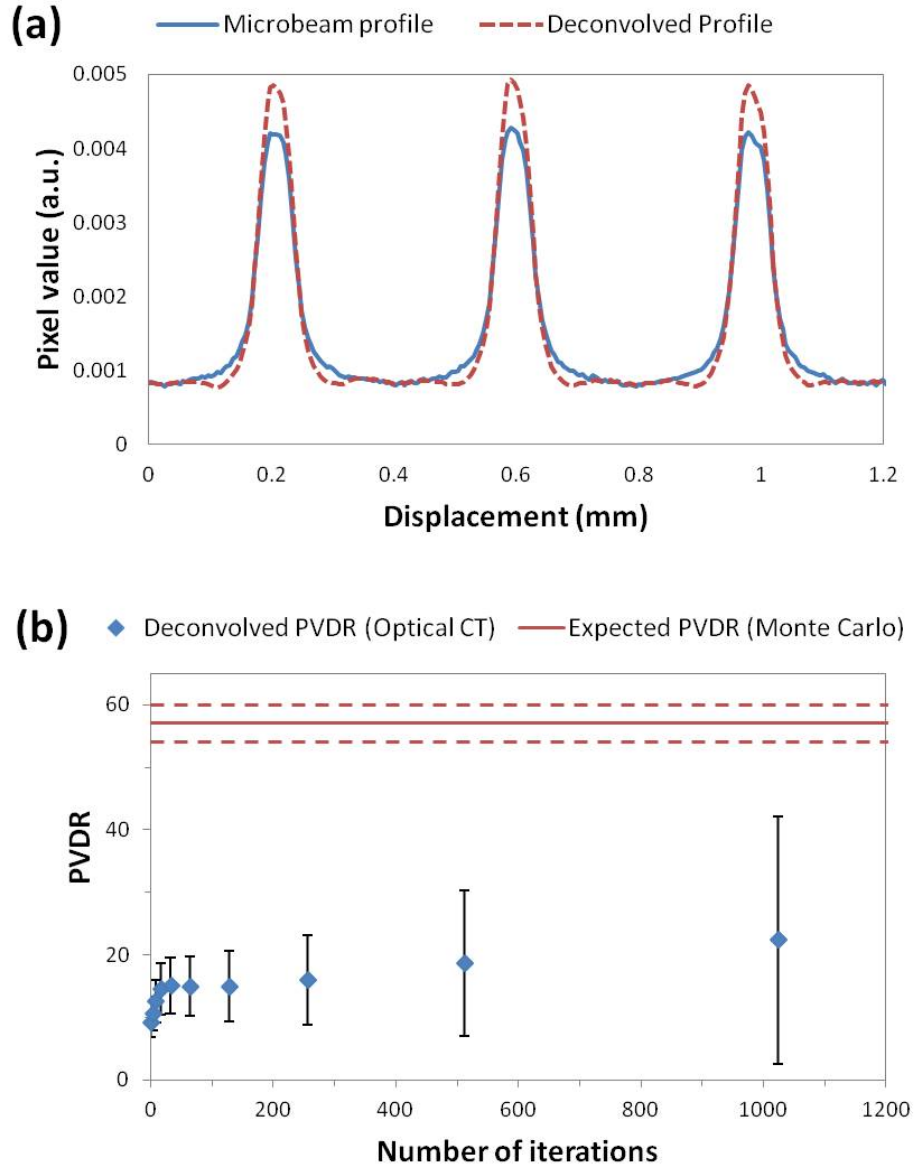
Figure 3.10. *a. A microbeam profile from sample 2.1 and the deconvolved profile after 4 iterations of Richardson-Lucy deconvolution using a PSF calculated from a 1 μm bead. This shows that deconvolution of the PSF improves the shape of the profile however, b. shows that the PVDR depends on the number of deconvolution iterations, which does not appear to converge before becoming extremely noisy. Therefore although deconvolution can qualitatively improve the images, we are hesitant to base any quantitative measurements on a deconvolved profile.*

the samples were refrigerated. The potential time-evolution of the measured doses is discussed in [Doran et al., 2013b] but whilst the error introduced at this step is expected to be significant, the pertinent observation for the purposes of this work is that PRESAGE® exhibits negligible diffusion of the dose-reporting chromophore. Thus, blurring of the microbeam dose due to the delay is not expected to have occurred.

The apparatus is sufficiently compact that a copy could be installed in the MRT hutch at ID-17. A number of improvements to the imaging methodology would be possible if the apparatus were located *in situ* at the beamline:

- As was discussed in [Doran et al., 2013b], pre-scanning the dosimeter would enable effects of refraction to be largely eliminated and an accurate zero-dose baseline to be established, for absolute measurements of valley dose given the new accurate positioning system.

- Images could be acquired within minutes of the end of the irradiation, eliminating any uncertainties caused by delayed readout, for example, related to time-evolution of the PRESAGE® dose-response [Skyt et al., 2011, Skyt et al., 2012].

- Further improvements in image SNR and extensions to the dynamic range of acquired data would be achievable via the acquisition of multiple datasets with different levels of illumination [Krstajic and Doran, 2007, Thomas et al., 2011b].

The results of Section 3.3 suggest that accurate PVDR measurements are not possible with the current optical CT arrangement. Given the results of the knife-edge measurements of MTF along the optical axis, we believe the underestimation of the PVDR by optical CT is primarily due to lack of true spatial resolution. Attempts to improve the resolution by increasing the numerical aperture and deconvolution using a measured PSF lead to unreliable and noisy results, making these methods unsuitable for clinical measurements of PVDR.

It remains an open question as to whether the optical CT technique will in future prove capable of making measurements of PVDR that are competitive with other methods such as those employing 2-D TLD films or MOSFET detectors. There are two possible avenues to move forward with quantitative microbeam measurements using optical CT.

First, using a smaller sample would mean that both the necessary FOV and DOF can be decreased, making it possible to increase the magnification and resolution. Although this involves the sacrifice of spatial information across the beams, full depth information would still be retained. This would enable, among other things, measurement of the effects of scattering along the entire length of the microbeams, rather than simply at a single depth determined by the detector location.

Second, while the measured resolution of 21.5 ± 0.5 μm in projections with NA setting A1 is insufficient for sampling the peak dose, it should be sufficient for quantitatively measuring the valley dose, which is four times wider than the peak. Arguably, in terms of patient safety the valley dose is the most important factor, as once the peak is over a certain value, cell death will occur. Therefore, having a valley measurement in 3-D, in combination with an alternative 2-D measurement of the peak dose on entry, could be of significant interest to the MRT community.

[Could add results of most recent experiment of small dosimeters if they work.]

3.5 Conclusions

3-D images of geometrically sophisticated synchrotron microbeam therapy deliveries have been obtained. The most significant current limitation of the imaging technique as presented here is the available spatial resolution, which has been investigated in detail. Although the data presented here fall some way short of the dose quantification needed for complete verification, the measurements and visualisations have already demonstrated their utility by detecting deviations from a planned treatment (Figures 3.6, 3.7(b)) and shown clear potential for quantitative measurement of the biologically important valley dose.

Bibliography

[Abdul Rahman et al., 2011a] Abdul Rahman, A., Elke, B., Brochard, T., Adamovics, J., Clowes, S., Bradley, D., and Doran, S. J. (2011a). Sophisticated test objects for the quality assurance of optical computed tomography scanners. *Physics in medicine and biology*, 56(14):4177–4199.

[Abdul Rahman et al., 2011b] Abdul Rahman, A. T., Bräuer-Krisch, E., Brochard, T., Adamovics, J., Clowes, S. K., Bradley, D., and Doran, S. J. (2011b). Sophisticated test objects for the quality assurance of optical computed tomography scanners. *Physics in Medicine and Biology*, 56(14):4177–4199.

[Adamovics and Maryanski, 2003] Adamovics, J. and Maryanski, M. (2003). New 3d radiochromic solid polymer dosimeter from leuco dyes and a transparent polymeric matrix. In *Medical Physics*, volume 30, pages 1349–1349. AMER ASSOC PHYSICISTS MEDICINE AMER INST PHYSICS STE 1 NO 1, 2 HUNTINGTON QUADRANGLE, MELVILLE, NY 11747-4502 USA.

[Akselrod et al., 2006] Akselrod, G., Akselrod, M., Benton, E., and Yasuda, N. (2006). A novel al_2o_3 fluorescent nuclear track detector for heavy charged particles and neutrons. *Nuclear Instruments and Methods in Physics Research Section B: Beam Interactions with Materials and Atoms*, 247(2):295–306.

[Anderson et al., 2003] Anderson, H. L., Yap, J. T., Miller, M. P., Robbins, A., Jones, T., and Price, P. M. (2003). Assessment of pharmacodynamic vascular response in a phase i trial of combretastatin a4 phosphate. *Journal of clinical oncology : official journal of the American Society of Clinical Oncology*, 21(15):2823–2830.

[Annabell et al., 2012] Annabell, N., Yagi, N., Umetani, K., Wong, C., and Geso, M. (2012). Evaluating the peak-to-valley dose ratio of synchrotron microbeams using PRESAGE fluorescence. *Journal of synchrotron radiation*, 19(Pt 3):332–339.

[Appleby et al., 1987] Appleby, A., Christman, E., and Leghrouz, A. (1987). Imaging of spatial radiation dose distribution in agarose gels using magnetic resonance. *Medical physics*, 14(3):382–384.

[Asayesh et al., 2006] Asayesh, A., Sharpe, J., Watson, R. P., Hecksher-Sørensen, J., Hastie, N. D., Hill, R. E., and Ahlgren, U. (2006). Spleen versus pancreas: strict control of organ interrelationship revealed by analyses of bapx1/ mice. *Genes & Development*, 20(16):2208–2213.

[Baldock et al., 2010] Baldock, C., De Deene, Y., Doran, S., Ibbott, G., Jirasek, A., Lepage, M., McAuley, K., Oldham, M., and Schreiner, L. (2010). Polymer gel dosimetry. *Physics in medicine and biology*, 55(5):R1.

[Bassi et al., 2010] Bassi, A., Brida, D., D'Andrea, C., Valentini, G., Cubeddu, R., De Silvestri, S., and Cerullo, G. (2010). Time-gated optical projection tomography. *Optics letters*, 35(16):2732–2734.

[Bayreder et al., 2008] Bayreder, C., Schon, R., Wieland, M., Georg, D., Moser, E., and Berg, A. (2008). The spatial resolution in dosimetry with normoxic polymer-gels investigated with the dose modulation transfer approach. *Medical physics*, 35(5):1756–1769.

[Berg et al., 2004] Berg, A., Pernkopf, M., Waldhausl, C., Schmidt, W., and Moser, E. (2004). High resolution MR based polymer dosimetry versus film densitometry: a systematic study based on the modulation transfer function approach. *Physics in medicine and biology*, 49(17):4087–4108.

[Blasberg, 2003] Blasberg, R. (2003). Molecular imaging and cancer. *Molecular cancer therapeutics*, 2(3):335–43.

[Blattmann et al., 2005] Blattmann, H., Gebbers, J.-O., Bräuer-Krisch, E., Bravin, A., Le Duc, G., Burkard, W., Di Michiel, M., Djonov, V., Slatkin, D., Stepanek, J., et al. (2005). Applications of synchrotron x-rays to radiotherapy. *Nuclear Instruments and Methods in Physics Research Section A: Accelerators, Spectrometers, Detectors and Associated Equipment*, 548(1):17–22.

[Boone et al., 1986] Boone, J. M., Arnold, B. A., and Seibert, J. A. (1986). Characterization of the point spread function and modulation transfer function of scattered radiation using a digital imaging system. *Medical physics*, 13:254.

[Boot et al., 2008] Boot, M. J., Westerberg, C. H., Sanz-Ezquerro, J., Cotterell, J., Schweitzer, R., Torres, M., and Sharpe, J. (2008). In vitro whole-organ imaging: 4D quantification of growing mouse limb buds. *Nature Methods*, 5(7):609–612.

[Bräuer-Krisch et al., 2003] Bräuer-Krisch, E., Bravin, A., Lerch, M., Rosenfeld, A., Stepanek, J., Di Michiel, M., and Laissue, J. (2003). Mosfet dosimetry for microbeam radiation therapy at the european synchrotron radiation facility. *Medical*

physics, 30(4):583–589.

[Bräuer-Krisch et al., 2005a] Bräuer-Krisch, E., Bravin, A., Zhang, L., Siegbahn, E., Stepanek, J., Blattmann, H., Slatkin, D., Gebbers, J.-O., Jasmin, M., and Laissue, J. (2005a). Characterization of a tungsten/gas multislit collimator for microbeam radiation therapy at the european synchrotron radiation facility. *Review of scientific instruments*, 76(6):064303.

[Bräuer-Krisch et al., 2013] Bräuer-Krisch, E., Nemoz, C., Brochard, T., Berruyer, G., Renier, M., Pouyatos, B., and Serduc, R. (2013). The preclinical set-up at the id17 biomedical beamline to achieve high local dose deposition using interlaced microbeams. In *Journal of Physics: Conference Series*, volume 425, page 022001. IOP Publishing.

[Bräuer-Krisch et al., 2009] Bräuer-Krisch, E., Requardt, H., Brochard, T., Berruyer, G., Renier, M., Laissue, J., and Bravin, A. (2009). New technology enables high precision multislit collimators for microbeam radiation therapy. *Review of Scientific Instruments*, 80(7):074301.

[Bräuer-Krisch et al., 2005b] Bräuer-Krisch, E., Requardt, H., Régnard, P., Corde, S., Siegbahn, E., G, L., Brochard, T., Blattmann, H., Laissue, J., and Bravin, A. (2005b). New irradiation geometry for microbeam radiation therapy. *Physics in medicine and biology*, 50(13):3103–3111.

[Bräuer-Krisch et al., 2010] Bräuer-Krisch, E., Rosenfeld, A. B., Lerch, M. L., Petasecca, M., Akselrod, M., Sykora, J., Bartz, J., Ptaszkiewicz, M., Olko, P., and Berg, A. (2010). Potential high resolution dosimeters for MRT. *AIP Conference Proceedings*, 1266:89–97.

[Bräuer-Krisch et al., 2010] Bräuer-Krisch, E., Serduc, R., Siegbahn, E., Le Duc, G., Prezado, Y., Bravin, A., Blattmann, H., and Laissue, J. (2010). Effects of pulsed, spatially fractionated, microscopic synchrotron x-ray beams on normal and tumoral brain tissue. *Mutation research*, 704(1):160–166.

[Brown et al., 1992] Brown, C. S., Burns, D. H., Spelman, F. A., and Nelson, A. C. (1992). Computed tomography from optical projections for three-dimensional reconstruction of thick objects. *Applied optics*, 31(29):6247–6254.

[Chen et al., 2012] Chen, L., McGinty, J., Taylor, H. B., Bugeon, L., Lamb, J. R., Dallman, M. J., and French, P. M. W. (2012). Incorporation of an experimentally determined MTF for spatial frequency filtering and deconvolution during optical projection tomography reconstruction. *Optics Express*, 20(7):7323–7337.

[Chen et al., 2009] Chen, W.-S., Huang, R.-H., and Hsieh, L. (2009). Iris recognition using 3d co-occurrence matrix. In *Advances in Biometrics*, pages 1122–1131. Springer.

[Choi et al., 2005] Choi, B., Tsu, L., Chen, E., Ishak, T. S., Iskandar, S. M., Chess, S., and Nelson, J. S. (2005). Determination of chemical agent optical clearing potential using in vitro human skin. *Lasers in Surgery and Medicine*, 36(2):72–75.

[Clift et al., 2010] Clift, C., Thomas, A., Adamovics, J., Chang, Z., Das, I., and Oldham, M. (2010). Toward acquiring comprehensive radiosurgery field commissioning data using the presage®/optical-ct 3d dosimetry system. *Physics in medicine and biology*, 55(5):1279.

[Colas and Sharpe, 2009] Colas, J. F. and Sharpe, J. (2009). Live optical projection tomography. *Organogenesis*, 5(4):211–216.

[Crosbie et al., 2008] Crosbie, J., Svalbe, I., Midgley, S., Yagi, N., Rogers, P., and Lewis, R. (2008). A method of dosimetry for synchrotron microbeam radiation therapy using radiochromic films of different sensitivity. *Physics in medicine and biology*, 53(23):6861.

[Crosbie et al., 2010] Crosbie, J. C., Anderson, R. L., Rothkamm, K., Restall, C. M., Cann, L., Ruwanpura, S., Meachem, S., Yagi, N., Svalbe, I., Lewis, R. A., et al. (2010). Tumor cell response to synchrotron microbeam radiation therapy differs markedly from cells in normal tissues. *International Journal of Radiation Oncology* Biology* Physics*, 77(3):886–894.

[Cullis et al., 2006] Cullis, E. R., Kalber, T. L., Ashton, S. E., Cartwright, J. E., Griffiths, J. R., Ryan, A. J., and Robinson, S. P. (2006). Tumour overexpression of inducible nitric oxide synthase (iNOS) increases angiogenesis and may modulate the anti-tumour effects of the vascular disrupting agent ZD6126. *Microvascular research*, 71(2):76–84.

[Darrell et al., 2008] Darrell, A., Meyer, H., Marias, K., Brady, M., and Ripoll, J. (2008). Weighted filtered backprojection for quantitative fluorescence optical projection tomography. *Physics in Medicine and Biology*, 53(14):3863–3881.

[Dilmanian et al., 2008] Dilmanian, F. A., Romanelli, P., Zhong, Z., Wang, R., Wagshul, M. E., Kalef-Ezra, J., Maryanski, M. J., Rosen, E. M., and Anschel, D. J. (2008). Microbeam radiation therapy: Tissue dose penetration and banggel dosimetry of thick-beams array interlacing. *European journal of radiology*, 68(3):S129–S136.

[Doran et al., 2013a] Doran, S., Rahman, A. A., Bräuer-Krisch, E., Brochard, T., and Adamovics, J. (2013a). Ultra-high resolution optical ct dosimetry for the visualisation of synchrotron microbeam therapy doses. In *Journal of Physics: Conference Series*, volume 444, page 012074. IOP Publishing.

[Doran, 2009] Doran, S. J. (2009). The history and principles of optical computed tomography for scanning 3-D radiation dosimeters: 2008 update. *Journal of Physics: Conference Series*, 164:012020.

[Doran et al., 2013b] Doran, S. J., Abdul Rahman, A., Brauer-Krisch, E., Brochard, T., Adamovics, J., Nisbet, A., and Bradley, D. (2013b). Establishing the suitability of quantitative optical CT microscopy of PRESAGE® radiochromic dosimeters for the verification of synchrotron microbeam therapy. *Physics in medicine and biology*, 58(18):6279–6297.

[Doran et al., 2010a] Doran, S. J., Brochard, T., Adamovics, J., Krstajić, N., and Bräuer-Krisch, E. (2010a). An investigation of the potential of optical computed tomography for imaging of synchrotron-generated x-rays at high spatial resolution. *Physics in Medicine and Biology*, 55(5):1531–1547.

[Doran et al., 2010b] Doran, S. J., Brochard, T., Adamovics, J., Krstajic, N., and Elke, B. (2010b). An investigation of the potential of optical computed tomography for imaging of synchrotron-generated x-rays at high spatial resolution. *Physics in medicine and biology*, 55(5):1531–1547.

[Doran et al., 2001] Doran, S. J., Koerkamp, K. K., Bero, M. A., Jenneson, P., Morton, E. J., and Gilboy, W. B. (2001). A CCD-based optical CT scanner for high-resolution 3D imaging of radiation dose distributions: equipment specifications, optical simulations and preliminary results. *Physics in Medicine and Biology*, 46(12):3191–3213.

[Doubrovin et al., 2001] Doubrovin, M., Ponomarev, V., Beresten, T., Balatoni, J., Bornmann, W., Finn, R., Humm, J., Larson, S., Sadelain, M., Blasberg, R., and et al. (2001). Imaging transcriptional regulation of p53-dependent genes with positron emission tomography in vivo. *Proceedings of the National Academy of Sciences of the United States of America*, 98(16):93005.

[Evelhoch et al., 2004] Evelhoch, J. L., M, L. P., He, Z., Zachary, D., Polin, L., Corbett, T. H., Langmuir, P., Wheeler, C., Stone, A., Leadbetter, J., Ryan, A. J., Blakey, D. C., and Waterton, J. C. (2004). Magnetic resonance imaging measurements of the response of murine and human tumors to the vascular-targeting agent ZD6126. *Clinical cancer research : an official journal of the American Association for Can-*

cer Research, 10(11):3650–3657.

[Fauver et al., 2005a] Fauver, M., Seibel, E., Rahn, J., Meyer, M., Patten, F., Neu-
mann, T., and Nelson, A. (2005a). Three-dimensional imaging of single isolated
cell nuclei using optical projection tomography. *Optics express*, 13(11):4210–4223.

[Fauver et al., 2005b] Fauver, M., Seibel, E. J., Rahn, J. R., Meyer, M. G., Patten,
F. W., Neumann, T., and Nelson, A. C. (2005b). Three-dimensional imaging
of single isolated cell nuclei using optical projection tomography. *Opt. Express*,
13(11):4210–4223.

[Fei et al., 2012] Fei, P., Yu, Z., Wang, X., Lu, P. J., Fu, Y., He, Z., Xiong, J., and
Huang, Y. (2012). High dynamic range optical projection tomography (HDR-OPT).
Optics Express, 20(8):8824–8836.

[Gagliardi et al., 2015] Gagliardi, F. M., Cornelius, I., Blencowe, A., Franich, R. D.,
and Geso, M. (2015). High resolution 3d imaging of synchrotron generated mi-
crobeams. *Medical Physics*, 42(12):6973–6986.

[Gore et al., 1996] Gore, J., Ranade, M., Maryañski, M., and Schulz, R. (1996). Radi-
ation dose distributions in three dimensions from tomographic optical density scan-
ning of polymer gels: I. development of an optical scanner. *Physics in medicine and
biology*, 41(12):2695–2704.

[Gore et al., 1999] Gore, J. C., Ranade, M., and Maryanski, M. J. (1999). Radiation
dose distributions in three dimensions from tomographic optical density scanning of
polymer gels: I. Development of an optical scanner - Abstract - Physics in Medicine
and Biology - IOPscience. *Physics in medicine . . . .*

[Groom, 1987] Groom, A. (1987). The microcirculatory society eugene m. landis
award lecture. microcirculation of the spleen: new concepts, new challenges. *Mi-
crovascular research*, 34(3):269–289.

[Gross and Piwnica-Worms, 2005] Gross, S. and Piwnica-Worms, D. (2005). Spying
on cancer: molecular imaging in vivo with genetically encoded reporters. *Cancer
cell*, 7(1):5–15.

[Guffroy et al., 2004] Guffroy, M., Dally, C., Vrignaud, P., Beys, E., and Bissery, M.
(2004). Evaluation of tissue perfusion (tumor, spleen, heart) in mice after adminis-
tration of AVE8062, a tumor vascular-targeting agent. *Proceedings of the American
Association for Cancer Research*, 2004(1):1255.

[Guo et al., 2006] Guo, P., Adamovics, J., and Oldham, M. (2006). A practical three-

dimensional dosimetry system for radiation therapy. *Medical Physics*, 33(10):3962.

[Hanahan and Weinberg, 2000] Hanahan, D. and Weinberg, R. A. (2000). The hallmarks of cancer. *Cell*, 100(1):57–70.

[Haralick et al., 1973] Haralick, R. M., Shanmugam, K., and Dinstein, I. H. (1973). Textural features for image classification. *Systems, Man and Cybernetics, IEEE Transactions on*, 6:610–621.

[Häusler, 1972] Häusler, G. (1972). A method to increase the depth of focus by two step image processing. *Optics Communications*, 6(1):38–42.

[Hecht, 2002] Hecht, E. (2002). *Optics*. Addison-Wesley.

[Hecksher-Søorensen et al., 2004] Hecksher-Søorensen, J., Watson, R. P., Lettice, L. A., Serup, P., Eley, L., De Angelis, C., Ahlgren, U., and Hill, R. E. (2004). The splanchnic mesodermal plate directs spleen and pancreatic laterality, and is regulated by *Bapx1/Nkx3.2*. *Development*, 131(19):4665–4675.

[Heilemann et al., 2015] Heilemann, G., Georg, D., and Berg, A. (2015). Pushing the boundaries of spatial resolution in dosimetry using polymer gels and radiochromic films. In *Journal of Physics: Conference Series*, volume 573, page 012034. IOP Publishing.

[Hoffman, 2005] Hoffman, R. (2005). The multiple uses of fluorescent proteins to visualize cancer in vivo. *Nature reviews. Cancer*, 5(10):796–806.

[Hoffman, 2009] Hoffman, R. M. (2009). Imaging cancer dynamics in vivo at the tumor and cellular level with fluorescent proteins. *Clinical and Experimental Metastasis*, 26:345–355.

[Hörnblad et al., 2011] Hörnblad, A., Cheddad, A., and Ahlgren, U. (2011). An improved protocol for optical projection tomography imaging reveals lobular heterogeneities in pancreatic islet and -cell mass distribution. *Islets*, 3(4):204–208.

[Horsman and Murata, 2003] Horsman, M. R. and Murata, R. (2003). Vascular targeting effects of ZD6126 in a C3H mouse mammary carcinoma and the enhancement of radiation response. *International journal of radiation oncology, biology, physics*, 57(4):1047–1055.

[Hsieh, 2003] Hsieh, J. (2003). *Computed Tomography: Principles, Design, Artifacts, and Recent Advances*. SPIE Press monograph. SPIE Press.

[Huang et al., 1993] Huang, D., Swanson, E. A., Lin, C. P., Schuman, J. S., Stinson,

W. G., Chang, W., Hee, M. R., Flotte, T., Gregory, K., Puliafito, C. A., et al. (1993). *Optical coherence tomography*. PhD thesis, Massachusetts Institute of Technology, Whitaker College of Health Sciences and Technology.

[Hudson and Larkin, 1994] Hudson, H. and Larkin, R. (1994). Accelerated image reconstruction using ordered subsets of projection data. *Medical Imaging, IEEE Transactions on*, 13(4):601–609.

[Inoué and Spring, 1997a] Inoué, S. and Spring, K. R. (1997a). *Video Microscopy: The Fundamentals*. The Language of Science. Plenum Press.

[Inoué and Spring, 1997b] Inoué, S. and Spring, K. R. (1997b). Video microscopy: The fundamentals (the language of science).

[Islam et al., 2003] Islam, K. T. S., Dempsey, J. F., Ranade, M. K., Maryanski, M. J., and Low, D. A. (2003). Initial evaluation of commercial optical CT-based 3D gel dosimeter. *Medical Physics*, 30(8):2159.

[Kawata et al., 1990] Kawata, S., Nakamura, O., Noda, T., Ooki, H., Ogino, K., Kuroiwa, Y., and Minami, S. (1990). Laser computed-tomography microscope. *Applied optics*, 29(26):3805–3809.

[Kelly et al., 1998] Kelly, R. G., Jordan, K. J., and Battista, J. J. (1998). Optical CT reconstruction of 3D dose distributions using the ferrous–benzoic–xylenol (FBX) gel dosimeter. *Medical Physics*, 25(9):1741–50.

[Kim et al., 2008] Kim, E., Bowsher, J., Thomas, A. S., Sakhalkar, H., Dewhirst, M., and Oldham, M. (2008). Improving the quantitative accuracy of optical-emission computed tomography by incorporating an attenuation correction: application to HIF1 imaging. *Physics in Medicine and Biology*, 53(19):5371–5383.

[Krstajić and Doran, 2006] Krstajić, N. and Doran, S. J. (2006). Focusing optics of a parallel beam CCD optical tomography apparatus for 3D radiation gel dosimetry. *Physics in Medicine and Biology*, 51(8):2055–2075.

[Krstajić and Doran, 2007] Krstajić, N. and Doran, S. J. (2007). Characterization of a parallel-beam CCD optical-CT apparatus for 3D radiation dosimetry. *Physics in Medicine and Biology*, 52(13):3693–3713.

[Krstajic and Doran, 2007] Krstajic, N. and Doran, S. J. (2007). Characterization of a parallel-beam CCD optical-CT apparatus for 3D radiation dosimetry. *Physics in medicine and biology*, 52(13):3693–3713.

[Laissue et al., 2001] Laissue, J. A., Blattmann, H., Di Michiel, M., Slatkin, D. N.,

Lyubimova, N., Guzman, R., Zimmermann, W., Birrer, S., Bley, T., Kircher, P., et al. (2001). Weanling piglet cerebellum: a surrogate for tolerance to mrt (microbeam radiation therapy) in pediatric neuro-oncology. In *International Symposium on Optical Science and Technology*, pages 65–73. International Society for Optics and Photonics.

[Lerch et al., 2011] Lerch, M., Petasecca, M., Cullen, A., Hamad, A., Requardt, H., Bräuer-Krisch, E., Bravin, A., Perevertaylo, V., and Rosenfeld, A. B. (2011). Dosimetry of intensive synchrotron microbeams. *Radiation Measurements*, 46(12):1560–1565.

[Lorbeer et al., 2011] Lorbeer, R. A., Heidrich, M., Lorbeer, C., Ramírez Ojeda, D. F., Bicker, G., Meyer, H., and Heisterkamp, A. (2011). Highly efficient 3D fluorescence microscopy with a scanning laser optical tomograph. *Optics Express*, 19(6):5419–5430.

[Mao et al., 2008] Mao, Z., Zhu, D., Hu, Y., Wen, X., and Han, Z. (2008). Influence of alcohols on the optical clearing effect of skin in vitro. *Journal of Biomedical Optics*, 13(2):021104–021104.

[Martínez-Rovira et al., 2012] Martínez-Rovira, I., Sempau, J., and Prezado, Y. (2012). Development and commissioning of a monte carlo photon beam model for the forthcoming clinical trials in microbeam radiation therapy. *Medical physics*, 39(1):119–131.

[Maryanski et al., 1993] Maryanski, M. J., Gore, J. C., Kennan, R. P., and Schulz, R. J. (1993). Nmr relaxation enhancement in gels polymerized and cross-linked by ionizing radiation: a new approach to 3d dosimetry by mri. *Magnetic resonance imaging*, 11(2):253–258.

[Maryanski et al., 1999] Maryanski, M. J., Zastavker, Y. Z., and Gore, J. C. (1999). Radiation dose distributions in three dimensions from tomographic optical density scanning of polymer gels: Ii. optical properties of the bang polymer gel. *Physics in medicine and biology*, 41(12):2705.

[McGinty et al., 2008] McGinty, J., Tahir, K. B., Laine, R., Talbot, C. B., Dunsby, C., Neil, M. A. A., Quintana, L., Swoger, J., Sharpe, J., and French, P. M. W. (2008). Fluorescence lifetime optical projection tomography. *Journal of Biophotonics*, 1(5):390–394.

[McGinty et al., 2011] McGinty, J., Taylor, H. B., Chen, L., Bugeon, L., Lamb, J. R., Dallman, M. J., and French, P. M. W. (2011). In vivo fluorescence lifetime optical

projection tomography. *Biomedical optics express*, 2(5):1340–1350.

[McGrath et al., 2010] McGrath, J., Drummond, G., McLachlan, E., Kilkenny, C., and Wainwright, C. (2010). Guidelines for reporting experiments involving animals: the arrive guidelines. *British journal of pharmacology*, 160(7):1573–1576.

[Natterer, 2001] Natterer, F. (2001). *The Mathematics of Computerized Tomography*. Classics in Applied Mathematics. Society for Industrial and Applied Mathematics.

[Oldham, 2004] Oldham, M. (2004). Optical-CT scanning of polymer gels. *Journal of Physics: Conference Series*, 3:122–135.

[Oldham et al., 2008a] Oldham, M., Sakhalkar, H., Oliver, T., Allan Johnson, G., and Dewhirst, M. (2008a). Optical clearing of unsectioned specimens for three-dimensional imaging via optical transmission and emission tomography. *Journal of Biomedical Optics*, 13(2):021113.

[Oldham et al., 2008b] Oldham, M., Sakhalkar, H., Oliver, T., Allan Johnson, G., and Dewhirst, M. (2008b). Optical clearing of unsectioned specimens for three-dimensional imaging via optical transmission and emission tomography. *Journal of biomedical optics*, 13(2):021113.

[Oldham et al., 2006] Oldham, M., Sakhalkar, H., Oliver, T., Wang, Y. M., Kirkpatrick, J., Cao, Y., Badea, C., Johnson, G. A., and Dewhirst, M. (2006). Three-dimensional imaging of xenograft tumors using optical computed and emission tomography. *Medical Physics*, 33(9):3193.

[Oldham et al., 2007a] Oldham, M., Sakhalkar, H., Wang, Y. M., Guo, P., Oliver, T., Bentley, R., Vujaskovic, Z., and Dewhirst, M. (2007a). Three-dimensional imaging of whole rodent organs using optical computed and emission tomography. *Journal of Biomedical Optics*, 12(1):014009.

[Oldham et al., 2007b] Oldham, M., Sakhalkar, H., Wang, Y. M., Guo, P., Oliver, T., Bentley, R., Vujaskovic, Z., and Dewhirst, M. (2007b). Three-dimensional imaging of whole rodent organs using optical computed and emission tomography. *Journal of biomedical optics*, 12(1):014009.

[Oldham et al., 2003] Oldham, M., Siewerdsen, J. H., Kumar, S., Wong, J., and Jaffray, D. A. (2003). Optical-CT gel-dosimetry I: basic investigations. *Medical Physics*, 30(4):623.

[Oldham et al., 2001] Oldham, M., Siewerdsen, J. H., Shetty, A., and Jaffray, D. A. (2001). High resolution gel-dosimetry by optical-CT and MR scanning. *Medical*

Physics, 28(7):1436.

[Olding and Schreiner, 2011] Olding, T. and Schreiner, L. J. (2011). Cone-beam optical computed tomography for gel dosimetry II: imaging protocols. *Physics in Medicine and Biology*, 56(5):1259–1279.

[Padhani and Miles, 2010] Padhani, A. R. and Miles, K. A. (2010). Multiparametric Imaging of Tumor Response to Therapy. *Radiology*, 256(2):348–364.

[Ptaszkiewicz et al., 2008] Ptaszkiewicz, M., Braurer-Kirsch, E., Klosowski, M., Czopyk, L., and Olko, P. (2008). Tld dosimetry for microbeam radiation therapy at the european synchrotron radiation facility. *Radiation Measurements*, 43(2):990–993.

[Ragan et al., 1988] Ragan, D., Schmidt, E., IC, M., and Groom, A. (1988). Spontaneous cyclic contractions of the capillary wall in vivo, impeding red cell flow: a quantitative analysis. evidence for endothelial contractility. *Microvascular research*, 36(1):13–30.

[Ray and Semerjian, 1983] Ray, S. R. and Semerjian, H. G. (1983). Laser tomography for simultaneous concentration and temperature measurement in reacting flows. In *American Institute of Aeronautics and Astronautics, Thermophysics Conference, 18 th, Montreal, Canada*.

[Requardt et al., 2005] Requardt, H., Corde, S., Siegbahn, E., LeDuc, G., Brochard, T., Blattmann, H., Laissue, J., Bravin, A., et al. (2005). New irradiation geometry for microbeam radiation therapy. *Physics in medicine and biology*, 50(13):3103.

[Rivers and Gualda, 2009] Rivers, M. L. and Gualda, G. A. (2009). 'tomo_display' and 'vol_tools': IDL VM Packages for Tomography Data Reconstruction, Processing, and Visualization. *AGU Spring Meeting Abstracts*, page A6.

[Rosset et al., 2004] Rosset, A., Spadola, L., and Ratib, O. (2004). OsiriX: an open-source software for navigating in multidimensional DICOM images. *Journal of Digital Imaging*, 17(3):205–216.

[Russ, 2002] Russ, J. C. (2002). *The Image Processing Handbook*. Image Processing Handbook. Crc Press.

[Sakhalkar et al., 2009] Sakhalkar, H. S., Adamovics, J., Ibbott, G., and Oldham, M. (2009). A comprehensive evaluation of the PRESAGE/optical-CT 3D dosimetry system. *Medical Physics*, 36(1):71.

[Sakhalkar et al., 2007] Sakhalkar, H. S., Dewhirst, M., Oliver, T., Cao, Y., and Old-

ham, M. (2007). Functional imaging in bulk tissue specimens using optical emission tomography: fluorescence preservation during optical clearing. *Physics in Medicine and Biology*, 52(8):2035–2054.

[Sakhalkar and Oldham, 2008] Sakhalkar, H. S. and Oldham, M. (2008). Fast, high-resolution 3D dosimetry utilizing a novel optical-CT scanner incorporating tertiary telecentric collimation. *Medical Physics*, 35(1):101.

[Schreiner, 2004] Schreiner, L. (2004). Review of fricke gel dosimeters. In *Journal of Physics: Conference Series*, volume 3, page 9. IOP Publishing.

[Serduc et al., 2009] Serduc, R., Bräuer-Krisch, E., Bouchet, A., Renaud, L., Brochard, T., Bravin, A., Laissue, J. A., and Le Duc, G. (2009). First trial of spatial and temporal fractionations of the delivered dose using synchrotron microbeam radiation therapy. *Synchrotron Radiation*, 16(4):587–590.

[Serduc et al., 2010] Serduc, R., Elke, B., Siegbahn, E. A., Bouchet, A., Pouyatos, B., Carron, R., Pannetier, N., Renaud, L., Berruyer, G., Nemoz, C., Brochard, T., Rémy, C., Barbier, E. L., Bravin, A., Le Duc, G., Depaulis, A., Estève, F., and Laissue, J. A. (2010). High-precision radiosurgical dose delivery by interlaced microbeam arrays of high-flux low-energy synchrotron x-rays. *PloS one*, 5(2):e9028.

[Sharpe, 2002] Sharpe, J. (2002). Optical Projection Tomography as a Tool for 3D Microscopy and Gene Expression Studies. *Science*, 296(5567):541–545.

[Sharpe, 2003a] Sharpe, J. (2003a). Optical projection tomography as a new tool for studying embryo anatomy. *Journal of Anatomy*, 202(2):175–181.

[Sharpe, 2003b] Sharpe, J. (2003b). Optical projection tomography as a new tool for studying embryo anatomy. *Journal of anatomy*, 202(2):175–181.

[Sharpe et al., 2002] Sharpe, J., Ahlgren, U., Perry, P., Hill, B., Ross, A., Jacob, H., Baldock, R., and Davidson, D. (2002). Optical projection tomography as a tool for 3D microscopy and gene expression studies. *Science (New York, N.Y.)*, 296(5567):541–545.

[Shcherbo et al., 2007] Shcherbo, D., Merzlyak, E., Chepurnykh, T., Fradkov, A., Ermakova, G., Solovieva, E., Lukyanov, K., Bogdanova, E., Zaraisky, A., Lukyanov, S., and et al. (2007). Bright far-red fluorescent protein for whole-body imaging. *Nature methods*, 4(9):741–6.

[Siegbahn et al., 2009] Siegbahn, E., E, B., Bravin, A., Nettelbeck, H., Lerch, M., and Rosenfeld, A. (2009). MOSFET dosimetry with high spatial resolution in intense

synchrotron-generated x-ray microbeams. *Medical physics*, 36(4):1128–1137.

[Siegbahn et al., 2006] Siegbahn, E., Stepanek, J., E, B., and Bravin, A. (2006). Determination of dosimetrical quantities used in microbeam radiation therapy (MRT) with monte carlo simulations. *Medical physics*, 33(9):3248–3259.

[Skyt et al., 2011] Skyt, P. S., Balling, P., Petersen, J. B. B., Yates, E. S., and Muren, L. P. (2011). Temperature dependence of the dose response for a solid-state radiochromic dosimeter during irradiation and storage. *Medical physics*, 38(5):2806–2811.

[Skyt et al., 2012] Skyt, P. S., Wahlstedt, I., Muren, L. P., Petersen, J. B. B., and Balling, P. (2012). Temperature and temporal dependence of the optical response for a radiochromic dosimeter. *Medical physics*, 39(12):7232–7236.

[Soufan et al., 2003] Soufan, A. T., Ruijter, J. M., van den Hoff, M. J. B., de Boer, P. A. J., Hagoort, J., and Moorman, A. F. M. (2003). Three-dimensional reconstruction of gene expression patterns during cardiac development. *Physiological genomics*, 13(3):187–195.

[Tarte et al., 1996] Tarte, B. J., Jardine, P. A., and van Doorn, T. (1996). Laser-scanned agarose gel sections for radiation field mapping. *International Journal of Radiation Oncology* Biology* Physics*, 36(1):175–179.

[Tarte et al., 1997] Tarte, B. J., Jardine, P. A., van Doorn, T., Nitschke, K. N., and Poulsen, M. G. (1997). Development of a CCD array imaging system for measurement of dose distributions in doped agarose gels. *Medical Physics*, 24:1521.

[Thomas et al., 2010] Thomas, A., Bowsher, J., Roper, J., Oliver, T., Dewhirst, M., and Oldham, M. (2010). A comprehensive method for optical-emission computed tomography. *Physics in Medicine and Biology*, 55(14):3947–3957.

[Thomas et al., 2011a] Thomas, A., Newton, J., and Oldham, M. (2011a). A method to correct for stray light in telecentric optical-CT imaging of radiochromic dosimeters. *Physics in Medicine and Biology*, 56(14):4433–4451.

[Thomas et al., 2011b] Thomas, A., Pierquet, M., Jordan, K., and Oldham, M. (2011b). A method to correct for spectral artifacts in optical-CT dosimetry. *Physics in medicine and biology*, 56(11):3403–3416.

[Tuchin and Engineers, 2007] Tuchin, V. V. and Engineers, S. O. P.-O. I. (2007). *Tissue Optics: Light Scattering Methods and Instruments for Medical Diagnosis*. Press Monographs. SPIE/International Society for Optical Engineering.

[Tuchin et al., 2002] Tuchin, V. V., Xu, X., and Wang, R. K. (2002). Dynamic Optical Coherence Tomography in Studies of Optical Clearing, Sedimentation, and Aggregation of Immersed Blood. *Applied optics*, 41(1):258–271.

[Vargas et al., 1999] Vargas, G., Chan, E. K., Barton, J. K., Rylander, H. G., and Welch, A. J. (1999). Use of an Agent to Reduce Scattering. *Lasers in Surgery and Medicine*, 24(2):133–41.

[Varia et al., 1998] Varia, M., Calkins-Adams, D., Rinker, L., Kennedy, A., Novotny, D., Fowler, W., and Raleigh, J. (1998). Pimonidazole: a novel hypoxia marker for complementary study of tumor hypoxia and cell proliferation in cervical carcinoma. *Gynecologic oncology*, 71(2):270–277.

[Varosi and Landsman, 1993] Varosi, F. and Landsman, W. (1993). An idl based image deconvolution software package. In *Astronomical Data Analysis Software and Systems II*, volume 52, page 515.

[Vinegoni et al., 2008] Vinegoni, C., Pitsouli, C., Razansky, D., Perrimon, N., and Ntziachristos, V. (2008). In vivo imaging of Drosophila melanogaster pupae with mesoscopic fluorescence tomography. *Nature Methods*, 5(1):45–47.

[Walls et al., 2005] Walls, J. R., Sled, J. G., Sharpe, J., and Henkelman, R. M. (2005). Correction of artefacts in optical projection tomography. *Physics in Medicine and Biology*, 50(19):4645–4665.

[Walls et al., 2007] Walls, J. R., Sled, J. G., Sharpe, J., and Henkelman, R. M. (2007). Resolution improvement in emission optical projection tomography. *Physics in Medicine and Biology*, 52(10):2775–2790.

[Wang and Wang, 2006] Wang, Y. and Wang, R. (2006). Imaging using parallel integrals in optical projection tomography. *Physics in Medicine and Biology*, 51(23):6023–6032.

[Wang and Wang, 2007] Wang, Y. and Wang, R. K. (2007). Optimization of image-forming optics for transmission optical projection tomography. *Applied optics*, 46(27):6815–6820.

[Webb, 1996] Webb, R. H. (1996). Confocal optical microscopy. *Reports on Progress in Physics*, 59:427–471.

[Wen et al., 2009] Wen, X., Tuchin, V. V., Luo, Q., and Zhu, D. (2009). Controling the scattering of Intralipid by using optical clearing agents. *Physics in Medicine and Biology*, 54(22):6917–6930.

[Winfree et al., 1996a] Winfree, A. T., Caudle, S., Chen, G., McGuire, P., and Szilagyi, Z. (1996a). Quantitative optical tomography of chemical waves and their organizing centers. *Chaos: An Interdisciplinary Journal of Nonlinear Science*, 6(4):617–626.

[Winfree et al., 1996b] Winfree, A. T., Caudle, S., Chen, G., P., M., and Szilagyi, Z. (1996b). Quantitative optical tomography of chemical waves and their organizing centers. *Chaos (Woodbury, N.Y.)*, 6(4):617–626.

[Wolodzko et al., 1999] Wolodzko, J. G., Marsden, C., and Appleby, A. (1999). CCD imaging for optical tomography of gel radiation dosimeters. *Medical Physics*, 26:2508.

[Workman et al., 2010] Workman, P., Aboagye, E., Balkwill, F., Balmain, A., Bruder, G., Chaplin, D., Double, J., Everitt, J., Farningham, D., Glennie, M., et al. (2010). Guidelines for the welfare and use of animals in cancer research. *British journal of cancer*, 102(11):1555–1577.

[Xia et al., 1995] Xia, W., Lewitt, R., and Edholm, P. (1995). Fourier correction for spatially variant collimator blurring in spect. *Medical Imaging, IEEE Transactions on*, 14(1):100–115.

[Xu et al., 2003] Xu, Y., Wuu, C., and Maryanski, M. J. (2003). Determining optimal gel sensitivity in optical CT scanning of gel dosimeters. *Medical Physics*, 30(8):2257.

[Xu et al., 2004] Xu, Y., Wuu, C. S., and Maryanski, M. J. (2004). Performance of a commercial optical CT scanner and polymer gel dosimeters for 3-D dose verification. *Medical Physics*, 31(11):3024.

[Yeh et al., 2003] Yeh, A. T., Choi, B., Nelson, J. S., and Tromberg, B. J. (2003). Reversible Dissociation of Collagen in Tissues. *The Journal of Investigative Dermatology*, 121(6):1332–5.

[Zhu et al., 2013] Zhu, D., Larin, K. V., Luo, Q., and Tuchin, V. V. (2013). Recent progress in tissue optical clearing. *Laser & photonics reviews*, 7(5):732–757.